biosensors

MDPI

Article

Dual-Channel Stopped-Flow Apparatus for Simultaneous Fluorescence, Anisotropy, and FRET Kinetic Data Acquisition for Binary and Ternary Biological Complexes

Roberto F. Delgadillo [1,2,3,*,†], Katie A. Carnes [4], Nestor Valles-Villarreal [2], Omar Olmos [2], Kathia Zaleta-Rivera [5] and Lawrence J. Parkhurst [1,*]

1 Department of Chemistry, University of Nebraska-Lincoln, Lincoln, NE 68588-0304, USA
2 School of Engineering and Sciences, Tecnologico de Monterrey, Monterrey, NL 64849, Mexico; nestor.valles@tec.mx (N.V.-V.); oolmos@tec.mx (O.O.)
3 BASF Enzymes LLC, 3550 John Hopkins Ct, San Diego, CA 92121, USA
4 GlaxoSmithKline, Medicinal Science and Technology, R&D, King of Prussia, PA 19406, USA; katie.x.carnes@gsk.com
5 Department of Bioengineering, University of California San Diego, San Diego, CA 92093, USA; kzaletar@eng.ucsd.edu
* Correspondence: delgadillo@tec.mx (R.F.D.); lparkhurst1@unl.edu (L.J.P.); Tel.: +1-650-804-1450 (R.F.D.); +1-402-472-3316 (L.J.P.)
† Current address: BASF Enzymes LLC, 3550 John Hopkins Ct, San Diego, CA 92121, USA.

Received: 30 September 2020; Accepted: 2 November 2020; Published: 19 November 2020

Abstract: The Stopped-Flow apparatus (SF) tracks molecular events by mixing the reactants in sub-millisecond regimes. The reaction of intrinsically or extrinsically labeled biomolecules can be monitored by recording the fluorescence, $F(t)$, anisotropy, $r(t)$, polarization, $p(t)$, or FRET, $F(t)_{FRET}$, traces at nanomolar concentrations. These kinetic measurements are critical to elucidate reaction mechanisms, structural information, and even thermodynamics. In a single detector SF, or L-configuration, the $r(t)$, $p(t)$, and $F(t)$ traces are acquired by switching the orientation of the emission polarizer to collect the I_{VV} and I_{VH} signals however it requires two-shot experiments. In a two-detector SF, or T-configuration, these traces are collected in a single-shot experiment, but it increases the apparatus' complexity and price. Herein, we present a single-detector dual-channel SF to obtain the $F(t)$ and $r(t)$ traces simultaneously, in which a photo-elastic modulator oscillates by 90° the excitation light plane at a 50 kHz frequency, and the emission signal is processed by a set of electronic filters that split it into the $r(t)$ and $F(t)$ analog signals that are digitized and stored into separated spreadsheets by a custom-tailored instrument control software. We evaluated the association kinetics of binary and ternary biological complexes acquired with our dual-channel SF and the traditional methods; such as a single polarizer at the magic angle to acquire $F(t)$, a set of polarizers to track $F(t)$, and $r(t)$, and by energy transfer quenching, $F(t)_{FRET}$. Our dual-channel SF economized labeled material and yielded rate constants in excellent agreement with the traditional methods.

Keywords: stopped-flow; kinetics; fluorescence; anisotropy; polarizers; magic angle; FRET; trFRET; L-type instrumentation; steady-state anisotropy

1. Introduction

The fast-mixing apparatus was designed to track fast reactions in solution and it has played a fundamental role in chemistry, biochemistry, and molecular biology to reveal molecular interactions of

proteins, DNA, RNA, enzymes, vitamins, or any other biomolecules that can be used as biosensors [1–4]. The Stopped-Flow (SF) origins began in 1923 with the continuous flow mixer of Hartridge and Roughton, but it required large-volume samples to have practical applications in molecular biology [5]. However, later modifications were introduced by Britton Chance to preserve material by accommodating small reaction volumes below ~500 µL [6]. In 1950, Quentin Gibson introduced a stopping syringe and a double mixer to properly invent the first SF [7]. Later, Robert Berger contributed with the high efficient ball mixer [8] that brought the mixing dead time in the sub-millisecond range [9]. Lastly, the last modern breakthrough was made by Gibson's lab when the first computer-controlled SF system was introduced [7].

The natural fluorescence or the artificial labeling of biomolecules by fluorescent dyes allows one to tract association and dissociation reactions in the SF apparatus by following the fluorescence quenching or enhancement, *F(t)*, and the changes in the rotation of the dye-attached molecule by anisotropy, *r(t)*, and polarization, *p(t)* [10]. In addition, the SF apparatus can track Förster Resonance Energy Transfer, $F(t)_{FRET}$, when an appropriated dye-pair is attached to each of the reactants or in the same molecule when conformational changes exist during binding [11]. In the *p(t)* case, it has been used to detect drugs of abuse [12–14], and the pesticide atrazine [15]. However, the *p(t)* signal is not a fundamental function and can lead to calculation errors; in contrast, the *r(t)* is a fundamental expression that is normalized to the total *F(t)* signal [16]. However, when *F(t)* varies due to changes in the dye quantum yield, *QY*, it is required to analyze the traces by following the product of *r(t)* and *F(t)* or *rF(t)* since it corrects the distortions and the kinetic traces can follow the exponential-decay behaviors [17].

Thus, when a single detection is used, the *r(t)* and *p(t)* sensing modalities are collected by alternating the position of the emission from vertical (I_{VV} or $I_{\parallel}$) to horizontal (I_{VH} or $I_{\perp}$)with respect to the excitation polarizer, however, in a two-detector apparatus, the I_{VV} and I_{VH} are recorded simultaneously [18]. These two types of configurations are known as L-format and T-format SF, respectively. The former requires a double amount of the reactant solutions to acquire sequentially the I_{VV} and I_{VH} traces, making the L-format very wasteful of valuable material [19]. On the other hand, the T-format is more expensive but practical, and it has been employed with success to study the refolding and unfolding of several proteins and enzymes [17,20,21], and to measure the association and dissociation rate constants of several biomolecules [22–27]

Therefore, preserve valuable material, we have modified an L-type SF to collect simultaneously the I_{VV} and I_{VH} signals with a single experimental shot by using electronic filters and an instrument control system, which sorts out the *F(t)* and *r(t)* kinetic traces and stores them in spreadsheets for the corresponding analysis. Our dual-channel SF makes use of a photoelastic modulator (PEM) that vibrates at 50 kHz to modulate the vertical-polarized excitation laser-beam into circularly polarized light [28]. The PEM was first employed by J. Wampler and R. Desa for steady-state fluorimetry [29]. Later, Giblin-Parkhurst modified the PEM position for better signal gain to study the kinetic rates of the ribosome and the initiation factor 3 [1,30].

To corroborate the fidelity of the dual-channel SF, we tested the electronic circuit and the custom-tailored instrument control software by collecting the association traces of Oregon green® biocytin (BcO) to avidin (AV) and compare them with the *F(t)* and *rF(t)* kinetic traces obtained with a set of two polarizers [19]. We further compare the dual-channel *F(t)* traces with the total fluorescein obtained with a single polarizer at the magic angle (54.7°) [18]. We continue testing the linearity of the instrument response for BcO-AV reactions at several concentrations and temperatures. Furthermore, we measured, by the dual-channel *F(t)* and *rF(t)* sensing modalities, the association kinetics of several dye-labeled DNA probes bearing the Adenovirus major late promoter, (TATAAAG, AdMLP), and the full-length and its core (N-terminal truncated) yeast Tata Binding Protein (yTBP and cTBP, respectively) [2,31–33]. We contrasted these dual-channel acquired traces with the $F(t)_{FRET}$ traces obtained with a double-labeled AdMLP functioning as a FRET probe. In addition, we monitor the ternary complex formation with preformed TBP-AdMLP complex and the Transcription

Factor II A (TFIIA), which binds upstream of the TATA box and modulates conformation changes in the TFIID that enables promoter recognition and binding towards the formation of the Pre-Initiation Complex (PIC) which is required for the transcription initiation process [34–39].

2. Materials and Methods

2.1. Solution Conditions

All experiments were conducted in a buffered solution of 25 mM Tris, 100 mM KCl, 5 mM $MgCl_2$, 1 mM $CaCl_2$, and 2 mM DTT at pH. The SF reactions and steady-state experiments were acquired in a temperature range of 15 °C to 30 °C as indicated in each particular experiment. The temperature was controlled by a water bath (±0.02 °C) measured by a thermistor placed in the water bath of the temperature-controlled cuvette (Hellma Cells, Inc., Plainview, NY, USA).

2.2. Biological AV-BcO Materials

A summary of all association SF reactions is shown in Figure 1 and Table 1. The Oregon green® 488 biocytin (BcO, lot 40300A) was purchased from Invitrogen (Eugene, OR, USA) and avidin (AV, CAS 1405-69-2, lot 608540) from Calbiochem (La Jolla, CA, USA). For the SF experimentation, the BcO concentration was 20 nM after mixing, and 200 nM, 260 nM, 520 nM, and 1040 nM for AV (in biotin site basis). The BcO and AV solutions were placed in syringe 1 and 2, respectively.

2.3. Oligonucleotide Probe Design

The dye-labeled top strands and the corresponding complements were synthesized by TriLink Biotechnologies, Inc. (San Diego, CA, USA). All strands were both HPLC and PAGE purified and the correct labeling was confirmed by comparing the dye's peak absorbance ratios with respect to the 260 nm DNA absorbance [40]. The duplex DNA (ds) was prepared using a 10 × molar excess of complementary strands with a preincubation time of at least 20–30 min before reaction mixing. The dye-labeled top strand contained the TATAAAA box sequence from the Adenovirus Major Late Promoter (AdMLP) that is bound and bent by TBP [41]. Several dyes were used to label a 14-nucleotide top coding strand bearing the AdMLP ($AdMLP_{14ds}$) and giving fluorescent probes of different sensitivity (Table 1, Figure 1). These dyes were attached to the single-strand oligomer probes by six-carbon linkers at the 3′ end with fluorescein (3′-Fl), and at the 5′ end either with x-rhodamine (5′-Xr) or TAMRA (N, N, N′, N′-tetramethyl-6-carboxyrhodamine, 5′-Ta). After complement binding, the duplexed probes were named $AdMLP_{14ds}$*Fl, Xr*$AdMLP_{14ds}$, and Ta*$AdMLP_{14ds}$, respectively. A fourth single-labeled probe was a 31-nucleotide AdMLP sequence labeled with an internally labeled carboxy Fl attached to thymine (dT-Fl) by a nine-atom linker, which was named $AdMLP_{31ds}$*Fl_{int}, and was designed to accommodate simultaneously the TBP and TFIIA proteins (Table 1, Figure 1). A double-labeled probe, Xr*$AdMLP_{14ds}$*Fl, was designed as a FRET probe to yield the $F(t)_{FRET}$ trace that monitors the donor quenching by energy transfer caused by DNA bending during the cTBP and yTBP binding. All the preformed duplex probes were placed in syringe 1 with at least 20–30 min incubation to reach the desired temperature under the water bath. The concentration of single and double labeled duplexes for all the SF experiments varied from 20 nM to 60 nM and to make comparative analysis between these different methodologies, it was needed to keep the protein/probe ratio constant.

Table 1. Stopped-flow association reactions monitored by *F(t)*, *r(t)*, *rF(t)*, and $F(t)_{FRET}$ sensing modalities.

SF Methodology	Signal	Reaction	Syringe 1 [a]	Syringe 2
Magic angle	***F(t)***	**AV-BcO**	**BcO**	AV
Polarizers	***r(t), F(t), & rF(t)***	**AV-BcO**	**BcO**	AV
		yTBP-Ta*AdMLP$_{14ds}$*Fl	5′-**Xr***GGGCTATAAAAGGC***Fl**-3′ 3′-CCCGATATTTTCCG-5′	yTBP
		cTBP-Xr*AdMLP$_{14ds}$	5′-Xr*GGGCTATAAAAGGC***Fl**-3′ 3′-CCCGATATTTTCCG-5′	cTBP
Dual-Channel	***r(t), F(t), & rF(t)***	**AV-BcO**	**BcO**	AV
		yTBP-Ta*AdMLP$_{14ds}$	5′-**Ta***GGGCTATAAAAGGC-3′ 3′-CCCGATATTTTCCG-5′	yTBP
		yTBP-AdMLP$_{14ds}$*Fl	5′-GGGCTATAAAAGGC***Fl**-3′ 3′-CCCGATATTTTCCG-5′	yTBP
		yTBP-AdMLP$_{31ds}$*Fl$_{int}$	5′-GCGGGGAATTCCTATAAAAGAA(T-**Fl**)GTGCTGGG-3′ 3′-CGCCCCTTAAGGATATTTTCTTACACGACCC-5′	yTBP
		yTFIIA-yTBP-AdMLP$_{31ds}$*Fl$_{int}$ [b]	yTBP + 5′-GCGGGGAATTCCTATAAAAGAA(T-**Fl**)GTGCTGGG-3′ 3′-CGCCCCTTAAGGATATTTTCTTACACGACCC-5′	yTFIIA
FRET	$F(t)_{FRET}$	**yTBP-Xr*AdMLP$_{14ds}$*Fl**	5′-**Xr***GGGCTATAAAAGGC***Fl**-3′ 3′-CCCGATATTTTCCG-5′	yTBP
		cTBP-Xr*AdMLP$_{14ds}$*Fl	5′-**Xr***GGGCTATAAAAGGC***Fl**-3′ 3′-CCCGATATTTTCCG-5′	cTBP

[a] Labeled top strand and complement were preincubated before protein binding. [b] The TFIIA-TBP-AdMLP$_{31ds}$*Fl$_{int}$ ternary complex was monitored by pre-forming the yTBP-AdMLP$_{31ds}$*Fl$_{int}$ binary complex in syringe 1.

2.4. Transcription Factor Proteins

The full-length Tata Binding Protein and the COOH terminal domain (or core domine) from *Saccharomyces cerevisiae* referred to as yTBP and cTBP, respectively; were expressed in *Escherichia coli*, purified, and concentrated in 25 mM HEPES-KOH, 20% glycerol, 1 mM EDTA, 1 mM DTT, and 300 mM KCl (pH 7.9) [2,42]. Both protein activities were determined by a titration protocol as described previously [2,3]; thus, all concentrations are reported for active proteins. The cTBP final concentrations, after mixing, were 98 nM for the dual-channel SF experiments, and 43 nM, 86 nM, and 166 nM for the FRET SF experiments. For the yTBP, the final concentrations, after mixing, were 210 nM, 220 nM, 420 nM, and 500 nM. All the cTBP and yTBP solutions were placed in syringe 2. The TFIIA binding SF kinetics were obtained with a preincubated TBP-AdMLP$_{31ds}$ complex of 220 nM yTBP and 20 nM AdMLP$_{31ds}$*Fl$_{int}$ placed in syringe 1, and an 850 nM TFIIA solution placed in syringe 2, all final concentrations after mixing.

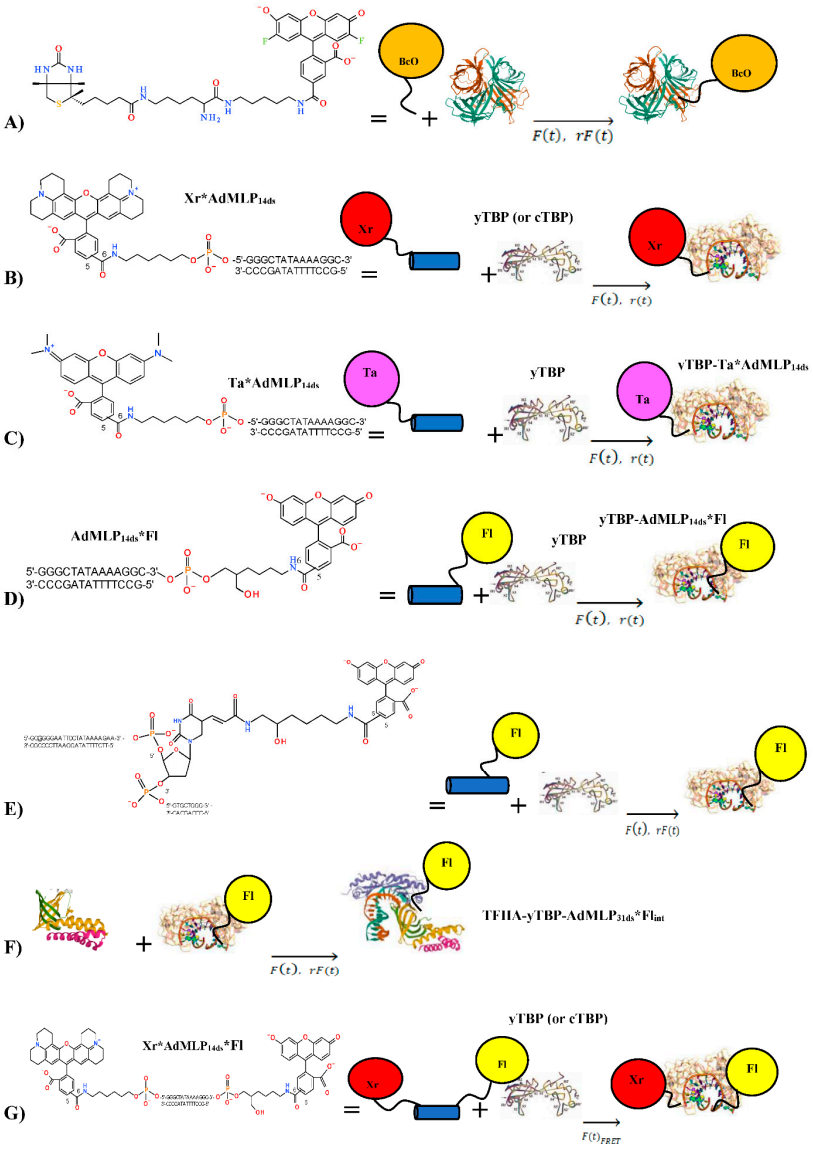

Figure 1. Stopped-flow association reactions monitored by *r(t)*, *F(t)*, *rF(t)*, *and* $F(t)_{FRET}$ sensing modalities. (**A**) The Oregon Green ® Biocytin (BcO) is attached through 18 non-hydrogen atoms as a spacer between the carboxy-dye and biotin ring structure, which binds to one of the four sites of avidin (AV) [43] under

pseudo-first-order condition (or > 10× binding site excess) [44]. (**B**–**G**) The Adenovirus Major Late promoter duplexed probes ($AdMLP_{ds}$, Table 1) are bound and bend by TATA-binding protein (TBP) [2,31]. To track the TBP-AdMLP association reactions, several duplex probes were used with three different dyes and two TATA bearing sequences of 14-nucleotide ($AdMLP_{14ds}$) and 31-nucleotide ($AdMLP_{31ds}$) oligomer lengths. (**B**) The $AdMLP_{14ds}$ probes were labeled at the 5′ end by x-rhodamine (Xr^*AdMLP_{14ds}), (**C**) TAMRA (Ta^*AdMLP_{14ds}), and (**D**) fluorescein at the 3′ end ($AdMLP_{14ds}{}^*Fl$). These 5′-Xr, 5-Ta, and 3′-Fl dyes were attached by six-carbon linkers. (**E**) The yTBP binding was also tracked with a fourth single labeled probe, a longer $AdMLP_{31ds}$ sequence, labeled internally by fluorescein ($AdMLP_{31ds}{}^*Fl_{int}$) attached by a nine-atom linker to the methyl group of the d-thymine (dT^*Fl_{int}) at position 23, and it was designed to accommodate at the same time the TBP and the TFIIA. (**F**) The extra space at the 5′ end allows us to obtain the TFIIA association rate constant when binding to a preformed yTBP-$AdMLP_{31ds}$ binary complex thus forming the ternary TFIIA-yTBP-$AdMLP_{31ds}{}^*Fl_{int}$ complex [45]. (**G**) The yTBP was also reacted with the double-labeled AdMLP duplex ($Xr^*AdMLP_{14ds}{}^*Fl$) to acquire the $F(t)_{FRET}$ traces as the inter-dye probe distance was decreased by the protein bending thus quenching the donor fluorescence signal.

2.5. Dual-Channel SF

The association reactions were collected in our custom-made SF apparatus (Figure 2) [2,46]. The fluorescence emission was collected with a 520-nm interference filter (10BPF10-520 Oriel Corp., Stratford, CT, USA) at 20–40 nM, after reaction mixing, for the BcO, $AdMLP_{14ds}{}^*Fl$, $Xr^*AdMLP_{14ds}{}^*Fl$, $AdMLP_{31ds}{}^*Fl_{int}$ probes, and the respective complexes. For the Ta^*AdMLP_{14ds} and Xr^*AdMLP_{14ds} probes, the emission signal was acquired by the 580-nm (10BPF10-580) and 620-nm interference filters, respectively (10BPF10-620, Oriel Corp., Stratford, CT), at 40 nM and 60 nM, respectively, after mixing (Figure 1, Table 1). The SF G-factor values were calculated with the half-wave plate and an emission polarizer to obtain the I_{HV}/I_{HH} ratio, at 520 nm for the BcO, $AdMLP_{14ds}{}^*Fl$, and $AdMLP_{31ds}{}^*Fl_{int}$ labeled probes and complexes, and at 580 nm and 620 nm for the Ta^*AdMLP_{14ds} and Xr^*AdMLP_{14ds} samples, respectively. The SF mixing dead time was 1 ms, and sufficient to detect a second-order rate constant of at least 1×10^9 $M^{-1}s^{-1}$. The excitation light was provided by a Coherent Ar^+ ion laser (Innova 70-4 Argon, Santa Clara, CA, USA) at 488 nm with an excitation power of 10–20 mW, for the BcO, $AdMLP_{14ds}{}^*Fl$, and $AdMLP_{31ds}{}^*Fl_{int}$ probes, and respective protein-probe complexes. For the Ta^*AdMLP_{14ds} and Xr^*AdMLP_{14ds} samples, the excitation was set at 514.5 nm with an excitation power of 135 mW. The laser source was followed by a photo-elastic modulator (PEM-80; HINDS International, Inc., Portland, OR, USA) oriented 45° with respect to the electric (E) vector of the incident light, and the half-wave modulation was set at 50 kHz (Figure 2).

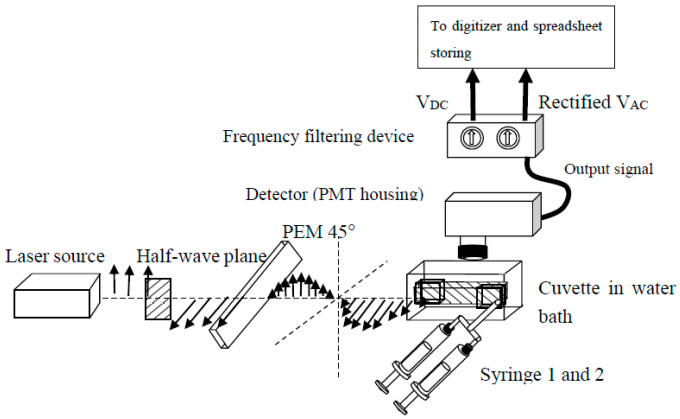

Figure 2. The modular dual-channel Stopped-Flow apparatus is equipped with a frequency rejection circuit for anisotropy, *r(t)*, and fluorescence, *F(t)*, detection. The optical train consists of the Coherent Ar^+ ion laser (Innova 70-4 Argon, Santa Clara, CA, USA) source, a half-wave plate, the PEM at 45° of the vertical electric vector, and the detector placed in an L-type configuration. The half-wave plate changes by 90° laser excitation plane just before being modulated by the PEM. The detector housing can accommodate interchangeable interference filters (e.g., 520 nm, 580 nm, and 620 nm) to collect the fluorescence emission

of the diverse dyes. The fluorescence emission is split into two signals, $V_{DC}(t)$ and rectified $V_{AC}(t)$, by the electronic filters to be later digitized and stored in spreadsheets to yield $r(t)$ and $F(t)$ according to Equation (7) and Equation (8), respectively. The temperature of the cuvette and syringes is controlled by a water bath from 10 °C to 30 °C. The syringes are simultaneously pushed by an air-controlled piston to deliver 150 µL solution each to be ball mixed with a 1 ms death time.

The dual-channel-SF filtering box consists of a 4-pole-pair digitally programmable band-pass (828BP), a passive high-pass filter with a set of capacitors, an active high-pass filter, a half-wave rectifier with negative output, and an integrator with capacitor selector (Figure 3). The demodulator circuitry provides a $V_{DC}(t)$ and a rectified $V_{AC}(t)$ voltage, yielding differing functions of the anisotropy as a function of time, $r(t)$, and the time-dependent total fluorescence, $F(t)$, by filtering out the desired frequency. The fluorescent signal is detected by R928 Photo-Multiplier Tube (PMT, Hamamatsu, Bridgewater, NJ, USA) having an emission spectral response of 185 to 900 nm, which is selected by an interference filter (520 nm, 580 or 620 nm, described above), and divided into two channels. The fluorescence light that passes the interference filter generates a voltage signal in the PMT that is fed as a "signal in" which is split into two signals. The first half-signal passes through an adjustable resister-capacitor filter (RC) to obtain a clean $V_{DC}(t)$ signal out. This RC filter has a variable capacitor set for the following time constants of 1 ms, 10 ms, 50 ms, 100 ms, and 500 ms and 1 s whose selection is equivalent to the time required for the capacitor voltage to decrease its initial voltage by up to 37%. The second split signal passes to an 828BP 4-pole-pair digitally programmable band-pass filter (Frequency Devices™, Inc., Ottawa, IL, USA) to isolate the 50 kHz signal that is transmitted to an active high-pass filter, consisting of an OP37 High-speed Operational Amplifier, and an *RC* filter with a resistance selector (*RC* filter with an adjustable time constant). Subsequently, the signal is conducted to a half-wave rectifier with negative output, consisting of an OP271 operational amplifier, a resistor set, and two rectifier diodes. Finally, the signal is fed to an integrator with a capacitor selector, consisting of an OP271 operational amplifier, a resistor, and a capacitor selector that yield the rectified $V_{AC}(t)$ signal.

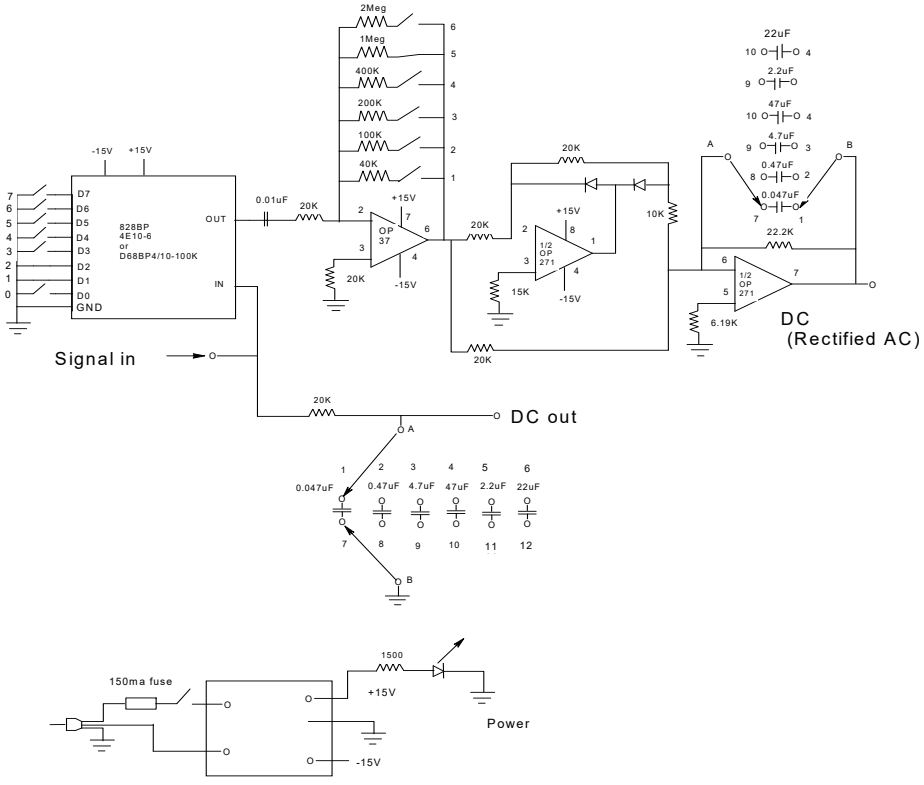

Figure 3. Circuit diagram for the dual-channel SF filtering box. The frequency selection circuitry filtered out the $r(t)$, and $F(t)$ traces by getting the ratio of $V_{AC}(t)/V_{DC}(t)$, according to Equation (7) and

Equation (8), respectively. The fluorescence emission that passes the interference filter (e.g., 520 nm, 580 nm, and 620 nm) produces a PMT analog signal (signal in) that is split into two, the first half goes through an adjustable resister-capacitor filter (*RC*) to obtain a clean $V_{DC}(t)$ signal out. This *RC* filter has a variable capacitor set for the following time constants of 1 ms, 10 ms, 50 ms, 100 ms, and 500 ms and 1 sec for the dials starting from 1 to 6. The second split signal passes through an 828BP 4-pole-pair digitally programmable band-pass filter (Frequency Devices ™, Inc.) to isolate the 50 kHz signal, which is then fed to an active high-pass filter and later to a half-wave rectifier with negative output. Finally, the signal is fed to an integrator with a capacitor selector to yield the $V_{AC}(t)$. The configuration of these electronic elements is powered by a 12V power supply. Further details are described in the text.

The effect of the PEM on the vertically polarized laser beam results in linear polarization, which is described by the Stokes' (*Sp*) vector (Equation (1)), and for the sake of simplicity, we assume unit irradiance, with periodic retardation, $\delta = \delta_0 \sin \omega t$, with scaling factor ($\delta_0$) and angular frequency (ω). At a $\pi/2$ scattering angle, the Stokes' vector for fluorescence (S_F) scattering is shown in Equation (2) [47], where the parameters F, I_0, and r account for fluorescence, incident light, and the anisotropy function, in that order.

$$S_P = \begin{pmatrix} 1 & 0 & 0 & 0 \\ 0 & \cos\delta & 0 & \sin\delta \\ 0 & 0 & 1 & 0 \\ 0 & -\sin\delta & 0 & \cos\delta \end{pmatrix} \begin{pmatrix} 1 \\ -1 \\ 0 \\ 0 \end{pmatrix} = \begin{pmatrix} 1 \\ -\cos\delta \\ 0 \\ \sin\delta \end{pmatrix} \quad (1)$$

$$S_F = \frac{F}{6I_0} \begin{pmatrix} 4-r & -3r & 0 & 0 \\ -3r & 3r & 0 & 0 \\ 0 & 0 & 0 & 0 \\ 0 & 0 & 0 & 0 \end{pmatrix} \begin{pmatrix} 1 \\ -\cos\delta \\ 0 \\ \sin\delta \end{pmatrix} = \frac{F}{6I_0} \begin{pmatrix} 4-r(1-3\ \cos\delta) \\ -3\,r\ (1+\cos\delta) \\ 0 \\ 0 \end{pmatrix} \quad (2)$$

The first term of the Stokes' vector gives the total irradiance due to *F* scattering. Thus, the instantaneous response in a photomultiplier detector (V) is proportional to this term, the sensitivity (S), and the transducer gain (κ) of the detector (Equation (3)):

$$V = \frac{\kappa\, S\, F}{6I_0}[4 - r(1 - 3\ \cos\delta)] \quad (3)$$

The averaged photomultiplier response over a PEM cycle becomes integrated by an RC filter of the demodulation circuitry resulting in direct current output, $V_{DC}(t)$ proportional to the $r(t)$ function (Equations (4) and (5)), and a rectified $V_{AC}(t)$ signal (Equation (6)) that together yield the anisotropy $r(t)$ (Equation (7)) and total fluorescence $F(t)$ information (Equation (8)).

$$V_{DC} = \frac{1}{t}\int_{t=0}^{t=k} V dt = \frac{\kappa\, S\, F}{6I_0}\{4 - r[1 - 3\ J_0(\delta_0)]\} \quad (4)$$

$$V_{DC} \sim F{\cdot}[1 - 0.47818{\cdot}\langle r\rangle{\cdot}(1 + 2.3806{\cdot}H)] \quad (5)$$

$$V_{AC} \sim 1.5\langle r\rangle_t F_t \quad (6)$$

where $H = (1 - G)/(1 + G)$ and $G = I_{HV}/I_{HH}$ is the SF grating factor, the instrument sensitivity ratio towards vertically and horizontally polarized light, which was obtained using an emission polarizer perpendicular and parallel to the electric (E) vector, respectively. The $V_{DC}(t)$ and $V_{AC}(t)$ were baseline corrected to obtain the respective ratio as a function of time (ρ_t) (Equation (7)) where the constant A_{Gain} is the instrumental amplitude gain, which was calculated solving $\rho(t)$ and $r(t)$ at $t = \infty$ which is

equivalent to r_{ss} of the complex. Finally, the total fluorescence signal *F(t)* is obtained after solving for the *r(t)* traces (Equation (8)).

$$\rho(t) = \frac{V_{AC}(t)}{V_{DC}(t)} = \frac{1.5 \cdot r(t) \cdot A_{Gain}}{1 - 0.47818 \cdot r(t) \cdot (1 + 2.3806 \cdot H)} \quad (7)$$

$$F(t) = \frac{V_{DC}(t)}{1 - 0.47818 \cdot r(t) \cdot (1 + 2.3806 \cdot H)} \quad (8)$$

The data acquisition was managed by an instrument control software (8.0 LabVIEW™) to sort each channel into two separate spreadsheets (Figure 4). The converted digital data was collected at a rate of 1530, 3060, or 6120 data points per second for 655 µs, 327 µs, and 163 µs separation per data points whose signals from each channel were baseline subtracted. The two analog signals from the demodulator were digitized by PCI-5122 high-speed digitizers from National Instruments (Austin, TX, USA) with a 14-bit resolution and 100 MHz bandwidth, through channel 0 and 1, the instrumental control panel of which is shown in Figure 5.

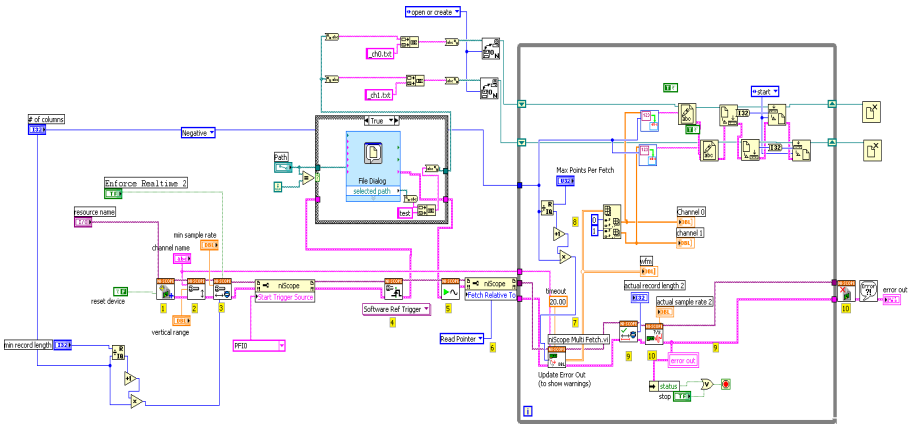

Figure 4. Schematic representation of the SF dual-channel LabView® instrument control software. The instrument virtual software prepares data acquisition to a sample rate of 1536, 3072, and 6144 data points per second and creates two text files to store the output $V_{DC}(t)$ and $V_{AC}(t)$ signals in channel 0 and 1, respectively. The virtual range corresponds to the voltage variation in the detector from -5V up to +5V. The collection protocol can be started manually or by a triggering signal (PF10) when the stopping syringe mechanism is closed (Figure 5). The waiting period for receiving the triggering signal is set at 20 s. When saturation is reached at 5V, the data acquisition is truncated. The background is collected with the buffer solution to eliminate it from the *r(t)* and *F(t)* traces.

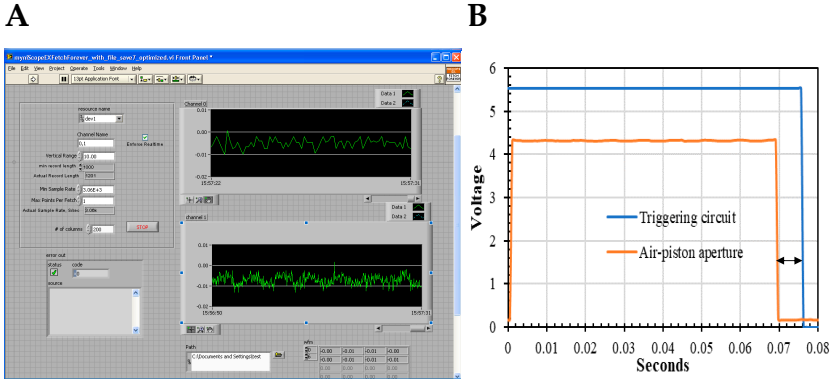

Figure 5. National Instrument front-screen interface for the dual-channel SF. (**A**) Channel 0 and channel 1 panels showing the $V_{DC}(t)$ and $V_{AC}(t)$ split signals, respectively, whose vertical range is 10 V from −5 V

to +5 V. The data speed acquisition was set at 1530, 3060, or 6120 data points per second in the "Min Sample Rate" input, which can be stored horizontally in columns, and are set in the "# of columns" input. (**B**) The triggering signal is received in the PFI0 input (Figure 4), which has a waiting time window of 20 s to initiate data collection. The aperture of the air piston pushes the two solution syringes in a 67 ms ± 1 ms window (orange line). The data-acquisition triggering is started by the stopping syringe mechanism that has a feedback signal (blue line) with a deadtime of 7 ms ± 1 ms with respect to the air-piston closure (double-arrow separation). In addition, data acquisition can be pre-triggered manually resulting in a death-time of ~1 ms, which depends on the ball mixing effectiveness.

2.6. Stopped-Flow Association Kinetics Acquired with Excitation and Emission Polarizers

The AV-BcO and yTBP-Ta*AdMLP$_{14ds}$ association reactions, at 20 °C and 25 °C, respectively, were acquired by the traditional two-polarizer method to compare the resulted kinetic traces with those acquired by the dual-channel SF. The two-polarizer SF experiments were carried out with the same apparatus already described but the analog PMT voltage is fed directly to the digitizer and without the need of the dual-channel filtering box. The concentration of AV and BcO solutions was 20 nM and 200 nM, respectively; and the Ta*AdMLP$_{14ds}$ and yTBP were 40 nM and 500 nM, respectively. The excitation wavelength was provided by the previously described Ar^+ laser, and the fluorescence emission was collected through the 520 nm and 580 nm interference filters described above. The time-dependent $I_{VV}(t)$ and $I_{VH}(t)$ traces were collected individually in two experiments yielding $r(t)$ according to Equation (9) [17], where G is the SF grating factor already described [19]. The $F(t)$ in Equation (10) corresponded to the denominator of Equation (9):

$$r(t) = \frac{I_{VV}(t) - G * I_{VH}(t)}{I_{VV}(t) + 2G * I_{VH}(t)} \quad (9)$$

$$F(t) = I_{VV}(t) + 2G * I_{VH}(t) \quad (10)$$

2.7. Stopped-Flow Association Kinetics Collected at the Magic Angle

The $F(t)$ association kinetics of BcO and AV reacting at concentrations of 20 nM and 200 nM, respectively, were also tracked with a single emission polarizer between the cuvette and the detector at the magic angle, $\theta = 54.74°$ [16,48]. The corresponding $F(t)$ intensity is three times smaller than the intensity in Equation (10); however, it must yield equivalent eigenvalues to describe the kinetic trace. The excitation was set at 488 nm provided by the described Ar^+ laser at 10–20 mW which polarization plane was orientated by a half-wave plate to be 90° with respect to the detector plane while the fluorescence emission was collected through the 520-nm interference filter previously described.

$$F(t) = 3 \cdot F(t)_{\theta=54.74°} \quad (11)$$

2.8. Steady-State Anisotropy, r_{ss}

The r_{ss} values of the free probes (e.g., BcO, Ta*AdMLP$_{14ds}$, etc.) and protein-probe complex (e.g., AV-BcO, yTBP-Ta*AdMLP$_{14ds}$, etc.) were collected with two polarizers or by the method of Giblin and Parkhurst (Equation (12)) [30]. The steady-state fluorescence signal was detected in a model A-1010 Alphascan fluorimeter (Photon Technologies, Inc.) equipped with an R928 PMT (Hamamatsu, Bridgewater, NJ, USA) with the emission-monochromator bandwidth set at 1 turn, and spectral response of 185 nm to 900 nm. For the polarizer method, the r_{ss} was calculated according to Equation (9). The excitation was provided by a Xenon arc set at 480 nm for the BcO, AdMLP$_{14ds}$*Fl, and AdMLP$_{31ds}$*Fl probes and complex samples. The 535 nm and 560 nm excitation wavelengths were used for the Ta*AdMLP$_{14ds}$ and Xr*AdMLP$_{14ds}$ probes and complex samples, respectively. For the Giblin-Parkhurst method, the excitation was provided by the 488 nm line of the Coherent® Ar^+ ion laser already described. The 514.5 nm excitation line was used for the Ta*AdMLP$_{14ds}$,Xr*AdMLP$_{14ds}$, and its respective protein-probe complexes. The Giblin-Parkhurst method required a PEM set 45°

with respect to the *E* vector of the laser beam and placed between the Coherent® Ar^+ ion laser and the sample compartment with a retardation level of 1.22·π. Two signals were obtained during 3–5 s with the power switch set at "on" and "off" position. The resulted signal was fitted to a straight line by the method of least squares to filter noise and photobleaching effects, yielding a ratio γ = on/off, that is used to calculate r_{ss} according to Equation (12):

$$r_{ss} = \frac{4 - 4\gamma}{\gamma 3(2 - 3H) + (1 - 3A + 3H + 3HB)} \quad (12)$$

where $H = (1 - G)/(1 + G)$, and G is the fluorimeter grating factor, $A = \int_{a=1.55}^{b=1.62} \cos(1.22\pi \cdot \sin x) \cdot H/\pi dx$, and $B = \int_{a=1.55}^{b=1.62} \sin(1.22\pi \cdot \sin x) \cdot H/\pi dx$. The r_{ss} values were calculated with at least six independent measurements at the reported temperatures in Table 2. The emission signals were selected by the fluorimeter's monochromator at 520 nm for BcO, $AdMLP_{14ds}$*Fl, and $AdMLP_{31ds}$*Fl probes and respective complexes. The fluorescence emission at 580 nm and 620 nm were collected for the Ta*$AdMLP_{14ds}$ and Xr*$AdMLP_{14ds}$ samples. The fluorimeter *G*-factor was obtained from 500–700 nm by measuring the I_{HV}/I_{HH} ratio acquired by polarizers with 3–5 s scans carried out by triplicated with a step size of 5–10 nm and the emission monochromator bandwidth set at 1 turn. The fluorimeter *G*-factor calculations required an $AdMLP_{14ds}$*Fl solution at a concentration of 0.5 μM, to yield the values in the 500–590 nm range. The fluorimeter *G*-factor in the 580–700 nm range was acquired by a solution of Xr*$AdMLP_{14ds}$ at a concentration of 4.7 μM at excitations of 510 nm and 560 nm.

Table 2. Steady-state anisotropy (r_{ss}) and quantum yield (*QY*) for unbound probes and complexes.

Sample	r_{ss} (Free Probe) [a]	r_{ss} (Complex) [b]	*QY* (Free Probe)	*QY* (Complex)
BcO (25 °C)	0.018 ± 0.001 [c] 0.025 ± 0.001 [d]	+AV: 0.180 ± 0.003 [c] +AV: 0.177 ± 0.004 [d]	0.91 ± 0.01	0.68 ± 0.02
BcO (20 °C)	0.025 ± 0.001 [d]	+AV: 0.185 ± 0.004 [d]		
BcO (15 °C)	0.054 ± 0.001 [d]	+AV: 0.176 ± 0.004 [d]		
BcO (10 °C)	0.055 ± 0.001 [d]	+AV: 0.202 ± 0.004 [d]		
Ta*$AdMLP_{14ds}$ (25 °C)	0.164 ± 0.002 [d]	+yTBP: 0.192 ± 0.010 [d]	0.20 ± 0.01	0.20 ± 0.01
Ta*$AdMLP_{14ds}$ (20 °C)	0.122 ± 0.002 [d]	+yTBP: 0.131 ± 0.005 [d]	0.20 ± 0.01	0.20 ± 0.01
$AdMLP_{14ds}$*Fl (20 °C)	0.071 ± 0.013 [d] 0.068 ± 0.008 [c]	+yTBP: 0.097 ± 0.002 [d]	0.22 ± 0.01	0.22 ± 0.01
Xr*$AdMLP_{4ds}$ (20 °C)	0.122 ± 0.003 [d] 0.122 ± 0.001 [c]	+cTBP: 0.130 ± 0.002 [d]	0.10 ± 0.01	0.10 ± 0.01
$AdMLP_{31ds}$*Fl_{int} (20 °C)	0.043 ± 0.004 [c] 0.040 ± 0.004 [d]	+yTBP: 0.201 ± 0.005 [d]	0.83 ± 0.03	0.71 ± 0.03
yTBP-$AdMLP_{31ds}$*Fl_{int} (17 °C)	0.201 ± 0.005 [d]	+yTFIIA: 0.260 ± 0.002 [d]	0.71 ± 0.03	0.82 ± 0.03
yTBP-$AdMLP_{31ds}$*Fl_{int} (25 °C)	0.198 ± 0.005 [d]	+yTFIIA: 0.217 ± 0.002 [d]	0.71 ± 0.03	0.72 ± 0.03

[a] The r_{ss} values were used to solve *r(t)* and *F(t)* in Equations (7) and (8), since the r_{ss} values of the free and bound probes corresponded to the association anisotropy traces at initial and endpoint, $r(t = 0)$, and $r(t = \infty)$, respectively. The unbound probes have low r_{ss} values since they are free to rotate; however, the anisotropy increased when the probe is bound in the complex. [b] Protein was added to at least 10× excess to reach at least 98% saturation of the fluorescent probe. [c] Calculated with polarizers. [d] Calculated with the method by Giblin-Parkhurst [30].

2.9. The F(t), r(t), and rF(t) Sensing Modalities Analysis

For the *F(t)* signal, the kinetic traces are dependent on the formation and disappearance of the involved fluorescence emitting species and their respective spectroscopy properties, according to Equation (13):

$$F(t) = \sum x_i(t)\varepsilon_{i(\lambda ex)}\cdot f_{i(\lambda ex)}\cdot QY_i = \sum x_i(t)\cdot QY_i^{eff} = \sum_1^2 x_i(t)\cdot \Delta QY \quad (13)$$

where x_i is the mole fraction of the fluorescence "i" species as a function of time (t), the $\varepsilon_{i(\lambda ex)}$ term is the molar extinction coefficient at the excitation wavelength, the $f_{i(\lambda \mathrm{em})}$ is the fluorescence spectral contour at the excitation wavelength, and the QY_i is quantum yield of the specie "i" [17]. Since the excitation wavelength is constant (e.g., 488 nm or 514.5 nm) and the emission is collected by an interference filter (e.g., 520 nm, 580 nm, or 620 nm), the last three terms can be grouped and simplified as the effective quantum yield, $QY_i^{eff} = \varepsilon_i(\lambda_{ex})\cdot f_i(\lambda_{ex})\cdot QY_i$. When i= 2, the QY_i^{eff} is equal to the QY difference between the free and bound probe in the complex, as following: $QY_i^{eff} = \Delta QY = QY_{free} - QY_{bound}$.

The *r(t)* signal depends on x_i, the specie's intrinsic anisotropy, r_i, and the respective QY_i value, as shown in Equation (14), where the denominator corresponds to Equation (13).

$$r(t) = \frac{\sum x_i(t)\cdot QY_i^{eff}\cdot r_i}{\sum x_i(t)\cdot QY_i^{eff}} = \frac{\sum_1^2 x_i(t)\cdot \Delta QY\cdot r_i}{\sum_1^2 x_i(t)\cdot \Delta QY} \quad (14)$$

In the case of large QY changes, the *r(t)* traces are distorted and do not follow the exponential decay models. However, the *r(t)* traces can be corrected by multiplying with the *F(t)* signals, resulting in a new function, *rF(t)*, as shown in Equation (15) [17]:

$$rF(t) = \sum x_i(t)\cdot QY_i^{eff}\cdot r_i = \sum_1^2 x_i(t)\cdot \Delta QY\cdot r_i \quad (15)$$

Since the three *F(t)*, *r(t)* and *rF(t)* sensing modalities have different amplitudes and values depending on the temperature and probe type (e.g., Fl, Xr, and Ta), it is better to normalize them to make a comparative analysis; which is denoted by a top bar, $\overline{r}(t)$, $\overline{F}(t)$ and $\overline{rF}(t)$, as shown in Equations (16)–(18), respectively:

$$\overline{r}(t) = (r(t) - r(0)) \;/\; (r(\infty) - r(0)) \quad (16)$$

$$\overline{F}(t) = (F(t) - F(\infty)) \;/\; (F(\infty) - F(0)) \quad (17)$$

$$\overline{rF}(t) = (rF(t) - rF(0)) \;/\; (rF(\infty) - rF(0)) \quad (18)$$

The *F(t)* kinetic traces were fitted to mono- and bi-exponential decays, e.g., $\overline{F}(t) = \alpha \times e(-\lambda \times t) + C$, $\overline{F}(t) = \alpha_1 \times e(-\lambda_1 \times t) + \alpha_2 \times e(-\lambda_2 \times t) + C$, respectively; where α is the pre-exponential and gives the relative phase contribution, where $\alpha_1 + \alpha_2 = 1$, λ is the eigenvalue with units of reciprocal seconds (s^{-1}), and C corresponds to a constant or baseline residual. In the case of other $\overline{r}(t)$ and $\overline{rF}(t)$ traces, the models are modified as following: $\overline{r}(t) = 1 - \alpha \times e(-\lambda \times t) + C$ and $\overline{r}(t) = 1 - [\alpha_1 \times e(-\lambda_1 \times t) + \alpha_2 \times e(-\lambda_2 \times t) + C]$, respectively.

2.10. Stopped-Flow Association Kinetics of TBP-AdMLP$_{14ds}$ Collected by Energy Transfer

The binding association of the yTBP and cTBP proteins to AdMLP$_{14ds}$ was tracked with the double-labeled Xr*AdMLP$_{14ds}$*Fl probe. The Fl donor emission was acquired with the previously described 520-nm interference filter yielding the $F(t)_{FRET}$ traces whose intensities decrease as the acceptor (Xr) gets closer to the Fl dye caused by the DNA bending as TBP binds to the probe [2,3,49]. In other

words, the $F(t)_{FRET}$ trace tracks the quenching of the donor as a function of the time due to the energy transfer towards the acceptor [2]. The $F(t)_{FRET}$ association traces were acquired in the previously described SF apparatus in which the analogous signal was fed directly to the digitizer. The resulted $F(t)_{FRET}$ traces were described by exponential decay models according to Equation (19). The excitation light was provided by the previously described Coherent Ar^+ ion laser at 488 nm and 10–20 mW power.

$$F(t)_{FRET} = \sum_{i=1}^{n} \alpha_i * e^{-\lambda_i * t} \tag{19}$$

2.11. Time-Resolved Energy Transfer, trFRET

To determine the DNA conformation changes caused by the TBP to two double-labeled $AdMLP_{14ds}$ probes (Ta*$AdMLP_{14ds}$*Fl and Xr*$AdMLP_{14ds}$*Fl), we measured the inter-dye distance (R) according to the FRET rate of transfer (k_t) which is inversely proportional to the reciprocal sixth power of interdye distance ($R^{1/6}$) as shown in Equation (20), where τ_D is the donor lifetime reference of 4.1 ns ± 0.1 ns and the R_0 is the Förster distance of 61.8 Å ± 1.7 Å and 65.3 Å ± 0.3 Å for Xr*$AdMLP_{14ds}$*Fl, and Ta*$AdMLP_{14ds}$*Fl, respectively [40]. The solution concentrations of the single labeled donor ($AdMLP_{14ds}$*Fl), and double-labeled Xr*$AdMLP_{14ds}$*Fl and Ta*$AdMLP_{14ds}$*Fl free probes were between 50–100 nM, and the respective complexes were formed by adding yTBP or cTBP to reach at least 1.5 µM to ensure >98% probe saturation, at 20 °C [3].

$$k_t = \frac{1}{\tau_D}\left(\frac{R_0}{R}\right)^6 \tag{20}$$

The time-resolved donor intensity in the nanosecond scale, $I_D(t)$, of the single-labeled unbound $AdMLP_{14ds}$*Fl and bound (yTBP-$AdMLP_{14ds}$*Fl or cTBP-$AdMLP_{14ds}$*Fl) complexes, were deconvoluted according to Equation (21), which yield τ_D or $<\tau_{Di}>$ for mono- or multiphasic decays, respectively. The excitation energy is lost by $<\tau_{Di}> = 1/k_{F(D)} = 1/({k_D}^0 + \Sigma k_{i(D)})$, which is the reciprocal of the sum of the natural fluorescence rate (${k_D}^0 = 1/{\tau}^0$) and the inactivation pathways ($\Sigma k_{i(D)}$). In addition, $<\tau_{Di}>$ is equal to $\Sigma\alpha_i\tau_i$, the sum of the area under the curve for each of the ith lifetimes with its respective fractional contribution (α_{Di}) so that $\Sigma\alpha_{Di} = 1$:

$$I_{Di}^{Exc/Emi}(t) = \sum_{i=1}^{n} \alpha_{Di} \cdot e^{-\left(\frac{t}{\langle\tau_{Di}\rangle}\right)} \tag{21}$$

The same time-resolved deconvolution model is used for the unbound and bound double-labeled duplexes, $I_{D(A)}(t)$, where A is the acceptor, and the fluorescence donor emission is collected by the 520-nm interference filter already described:

$$I_{Di(A)}^{Exc/Emi}(t) = \sum_{i=1}^{n} \alpha_{Di(A)} \cdot e^{-\left(\frac{t}{\langle\tau_{Di(A)}\rangle}\right)} \tag{22}$$

The deconvolution yielded the lifetimes of single and double-labeled duplexes, the $<\tau_{Di}>$ and $<\tau_{D(A)i}>$ respectively, of free and TBP bound samples. To obtain the interdye R (Equation (23)), the $<\tau_{Di}>$ is used as the donor reference lifetime for which the transfer rate constant (k_t) is optimized as a function of a distance distribution, denoted as $P(R)$ described by a mean inter-dye distance, $\overline{R}$, and a standard deviation, σ (Equation (24)). These two parameters of $P(R)$ are optimized using nonlinear regression algorithms or a method of moments [2] to match the observed donor decay in the presence of the acceptor, $<\tau_{D(A)i}>$.

$$I_{Di(A)}^{Exc/Emi}(t) = \int_0^{\infty} P(R) \sum_{i=1}^{n} \alpha_{Di} e^{\left[-\left({\tau_{Di}}^{-1} + k_t\right)\cdot t\right]} dR \tag{23}$$

$$P(R) = \frac{1}{\sigma\sqrt{2\pi}} \exp\left[-\left(R-\overline{R}\right)^2/\left(2\sigma^2\right)\right] \quad (24)$$

The corresponding DNA bend angle (α) was calculated according to Equation (25) in a simple rod model with two-kinks, based on the $\overline{R}$ for the free and bound double-labeled Xr*AdMLP$_{14ds}$*Fl and Ta*AdMLP$_{14ds}$*Fl probes [50].

$$\frac{\overline{R}_{bound}}{\overline{R}_{unbound}} = \frac{\left(\overline{R}_{free} - L_2\right)\cos(\propto/2) + L_2}{\overline{R}_{unbound}} \quad (25)$$

The raw I_D and $I_{D(A)}$ decays were acquired using a dye-tunable laser pumped by an N_2 LaserStrobe® spectrofluorometer (PTI, Photon Technologies, Inc., Birmingham, NJ, USA) with a 10 Hz pulsed excitation set at 481 nm provided by PLD481 dye (Photon Technologies, Inc.). The decays were collected by filtering donor fluorescence emission through a 520-nm interference filter (10BPF10-520, Oriel Corp., Stratford, CT, USA) preceded by a liquid filter containing a 1 cm path length of 24.1 mM acetate-buffered dichromate (pH 4) to remove extra scattered light that may pass the interference filter. Three successive replicate decays were collected and immediately averaged to yield one sample decay having 120 points with 30 excitation pulses per point. Two instrument response functions (IRF) were collected with a glycogen solution for deconvolution purposes, and six sample curves were collected per set. At least four sets of six decays per set were collected per sample, which were deconvoluted in the nanosecond (ns) range to mono- bi- and tri-exponential decay models (Equations (21) and (22)) which were discriminated depending on the selection criteria of χ^2 between 0.9–1.1 [51], the residual correlation Durbin-Watson (*DW*) above 1.5 [52], and the runs test *Z* [53].

3. Results and Discussions

3.1. Steady-State Anisotropy

The fluorimeter *G*-factor values are used to correct for the detector-sensitivity deviations at the three emission wavelengths (e.g., 520 nm, 580 nm, and 620 nm) (Table 2, Supplementary Materials Figure S1). The fluorimeter *G*-factor at 520 nm was 0.7933 ± 0.0128 (Figure S1), which is the emission wavelength for the BcO, AdMLP$_{14ds}$*Fl, and AdMLP$_{31ds}$*Fl$_{int}$ free probes and respective protein-bound complexes. The fluorimeter *G*-factor values, at 580 and 620 nm, were 0.6950 ± 0.0033 and 0.6388 ± 0.0134 at 620 nm, respectively (Figure S1), for the Ta*AdMLP$_{14ds}$ and Xr*AdMLP$_{14ds}$ labeled free and bound with TBP. Indeed, the free probes showed low r_{ss} values that increased when complexed with the proteins, and the complex r_{ss} values were used to solve for the association kinetic traces (Equation (7)) since they give the endpoint of the reaction at $r(t = \infty)$. To make sure it was calculated correctly, we added large excess of protein concentration until the r_{ss} value remained unchanged, indicating that the reaction was driven to completion. Thus, in all the cases, the reactions were carried out at pseudo-first-order conditions with a protein excess of 10×, for at least 98% probe saturation. We observed an r_{ss} temperature dependence in the BcO samples, from 10 °C, 15 °C, 20 °C, and 25 °C (Table 2), which was carefully determined to make a good kinetic comparative analysis.

3.2. Dual-Channel SF Validation by Polarizers and Magic Angle Methodologies

The association traces of BcO binding to AV were acquired with the *F(t)* and *r(t)* sensing modalities by the dual-channel SF methodology (Figure 6A–F) and the traditional two-polarizer method (Equations (9) and (10), Figure 6G,H). We also collected the *F(t)* with a single polarizer at the magic angle position (Equation (11)). For these three methodologies, the SF *G*-factor at 520 nm was 0.819 ± 0.015 (Figure S1). For the *F(t)* traces, the baseline-subtracted amplitudes were proportional to the change of the relative *QY* of the unbound and complex, $\Delta F = (QY_{unbound} - QY_{complex})$ (Table 2). Certainly, to make a comparison of the *F(t)* traces acquired at multiple excitation intensities and the *r(t)*

at different temperatures, all traces were normalized according to Equation (16) to Equation (18), yielding the $r(t)$, $\overline{F}(t)$, and $\overline{rF}(t)$, respectively.

Table 3. The eigenvalues (λ) and calculated association rate constants (k_{on}) of the association reaction of BcO (20 nM) and AV (200 nM) at 20 °C, obtained with the $\overline{F}(t)$ and $\overline{rF}(t)$ sensing modalities, and acquired by the tree stopped-flow methodologies.

Fluorescence, $\overline{F}(t)$ [a]	λ (s^{-1})	k_{on} ($\times 10^{-6}$ $M^{-1}s^{-1}$)	Error (%) [c]
Dual channel	1.186 ± 0.043	5.93 ± 0.22	3.6
Polarizers	1.187 ± 0.083	5.94 ± 0.42	7.0
Magic angle	1.199 ± 0.099	5.99 ± 0.60	8.3
$\overline{rF}(t)$ [b]	λ (s^{-1})	k_{on} ($\times 10^{-6}$ $M^{-1}s^{-1}$)	Error (%) [d]
Dual channel	1.183 ± 0.023	5.92 ± 0.12	2.0
Polarizers	1.198 ± 0.039	5.99 ± 0.20	3.3
Magic angle	NA	NA	NA

[a] The photobleaching was discarded from the reaction model. [b] The $\overline{rF}(t)$ is the product of $r(t) \times F(t)$, which corrects the distortion of the $r(t)$ traces by changes in the QY_i [17]. [c] The $\overline{F}(t)$ errors acquired by polarizers and magic angle methodologies were ~2× larger than the errors observed with the dual-channel and magic-angle SF methodology. [d] The $\overline{rF}(t)$ error acquired by polarizers was 1.65× larger than the error observer with the dual-channel methodology.

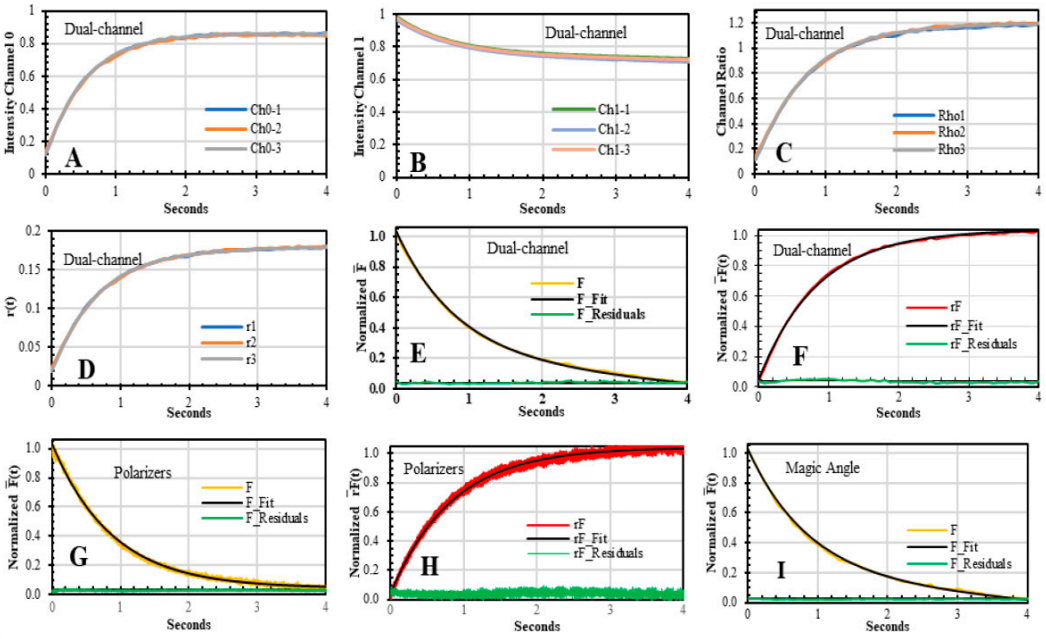

Figure 6. Stopped-flow kinetic traces acquired by dual-channel (**A**–**F**), polarizers (**G**,**H**), and magic-angle (**I**) methodologies for the binding association of BcO (20 nM) and AV (200 nM) at 20 °C. The $F(t)$ and $rF(t)$ sensing modalities were employed to track the AV-BcO complex formation. For the former trace, the ΔF decreased as the BcO fluorescence is quenched when the complex is formed and it is equivalent to ΔQY (Table 2), and in the case of the $rF(t)$, the trace value increased as the probe binds to the protein decreasing its rotation. (**A**,**B**) The dual-channel $V_{AC}(t)$ and $V_{DC}(t)$ traces were collected in channels 0 and 1, respectively. (**C**,**D**) The endpoint ratio of channel 0 and channel 1, $\rho(\infty)$= 1.2, and the r_{ss} of the AV-BcO complex are used to solve for the $r(t)$ traces according to Equation (7) (Table 2) to later obtain the $\overline{F}(t)$ (Equation (8)), and subsequently the $\overline{rF}(t)$ traces. (**E**) The $\overline{F}(t)$ traces were solved with

Equation (8) and the respective fitted curves (black line, and residual in green) yielded two eigenvalues of λ_1= 1.186 s^{-1} ± 0.046 s^{-1} and λ_2 = 0.02 ± 0.01 s^{-1} (Table 3). The latter λ corresponds to photobleaching and is neglected from further analysis. (**F**) The $\overline{rF(t)}$ fitting parameters yielded an λ = 1.183 s^{-1} ± 0.023 s^{-1} as the probe's rotation decreases in the newly formed complex. (**G**,**H**) The $\overline{F}(t)$ and $\overline{rF}(t)$ association traces acquired by polarizers yielded mono-exponential decays with λ_1 = 1.198 s^{-1} ± 0.039 s^{-1}, and λ_1 = 1.187s^{-1} ± 0.083 s^{-1}, respectively. The photobleaching was λ_2 = 0.02 s^{-1} ± 0.01 s^{-1}. (**I**) The $\overline{F}(t)$ traces collected by a single polarizer at the magic angle (54.7°) yielded λ_1 = 1.199 s^{-1} ± 0.099 s^{-1} and the photobleaching decay was λ_2 = 0.01 s^{-1} ± 0.01 s^{-1}.

The $\overline{F}(t)$ traces were better described by a bi-exponential model; however, the second phase, $\alpha_2 \times e(-\lambda_2/t)$, corresponded to photobleaching as shown by traces acquired by discontinuous excitation (Figure 7A,B). The photobleaching eigenvalue ranged from λ_2 = 0.01 s^{-1} to 0.02 s^{-1} depending on the laser intensity, and it is ignored in the data analysis. The kinetic traces were fitted to a reaction model of AV + BcO → AV−BcO, under pseudo-first-order condition (>10 × protein excess) after photobleaching was discarded. The biomolecular rate constant (k_{on}) was obtained with the reaction eigenvalue, $\lambda_1 = k'$[BcO], where $k' = k_{on}$[AV]. The k_{on} values calculated from the $\overline{F}(t)$ traces; acquired by the dual-channel, polarizers, and the single polarizer at the magic angle methodologies; were in excellent agreement with the overlapping errors (Table 3).

Table 4. Fitted eigenvalues (λ) and association rate constants (k_{on}) of AV-BcO as a function of concentration and temperature, at pH 8, and under pseudo-first-order conditions. [a.]

	200 nM		**260 nM**		**520 nM**		**1040 nM**		
λ(s^{-1})	$\overline{F}(t)$	$\overline{rF}(t)$	$\overline{F}(t)$	$\overline{rF}(t)$	$\overline{F}(t)$	$\overline{rF}(t)$	$\overline{F}(t)$	$\overline{rF}(t)$	
10 °C	NA	NA	0.629 ± 0.042	0.690 ± 0.035	1.355 ± 0.047	1.372 ± 0.003	2.825 ± 0.107	2.620 ± 0.012	
15 °C	NA	NA	1.058 ± 0.016	1.035 ± 0.005	1.840 ± 0.055	1.840 ± 0.009	4.000 ± 0.108	4.200 ± 0.365	
20 °C	1.186 ± 0.043	1.183 ± 0.023	1.491 ± 0.027	1.543 ± 0.014	3.045 ± 0.085	3.024 ± 0.030	6.209 ± 0.571	6.357 ± 0.058	
25 °C	NA	NA	2.465 ± 0.014	2.473 ± 0.018	4.920 ± 0.093	4.920 ± 0.034	10.031 ± 0.401	9.810 ± 0.091	
k_{on} $\times 10^{-6}$ $M^{-1}s^{-1}$	$\overline{F}(t)$	$\overline{rF}(t)$	$\overline{F}(t)$	$\overline{rF}(t)$	$\overline{F}(t)$	$\overline{rF}(t)$	$\overline{F}(t)$	$\overline{rF}(t)$	**k_{on} (Average)**
10 °C	NA	NA	2.419 ± 0.162	2.655 ± 0.133	2.606 ± 0.091	2.638 ± 0.006	2.520 ± 0.010	2.716 ± 0.012	2.592 ± 0.107
15 °C	NA	NA	4.069 ± 0.061	3.980 ± 0.021	3.539 ± 0.106	3.539 ± 0.018	3.846 ± 0.104	4.038 ± 0.351	3.835 ± 0.242
20 °C	5.931 ± 0.216	5.931 ± 0.117	5.733 ± 0.103	5.935 ± 0.054	5.855 ± 0.164	5.815 ± 0.058	5.970 ± 0.549	6.113 ± 0.056	5.904 ± 0.133
25 °C	NA	NA	9.479 ± 0.052	9.513 ± 0.068	9.461 ± 0.180	9.461 ± 0.066	9.646 ± 0.386	9.433 ± 0.088	9.499 ± 0.077

[a] The association reactions were acquired with BcO (20 nM) binding to AV at 200 nM, 260 nM, 520 nM, and 1040 nM concentrations from 10 °C to 25 °C at pH 8. The normalized $\overline{F}(t)$ and $\overline{rF}(t)$ sensing modalities yielded equivalent bimolecular rate constant (k_{on}) for the BcO binding to the AV at each temperature.

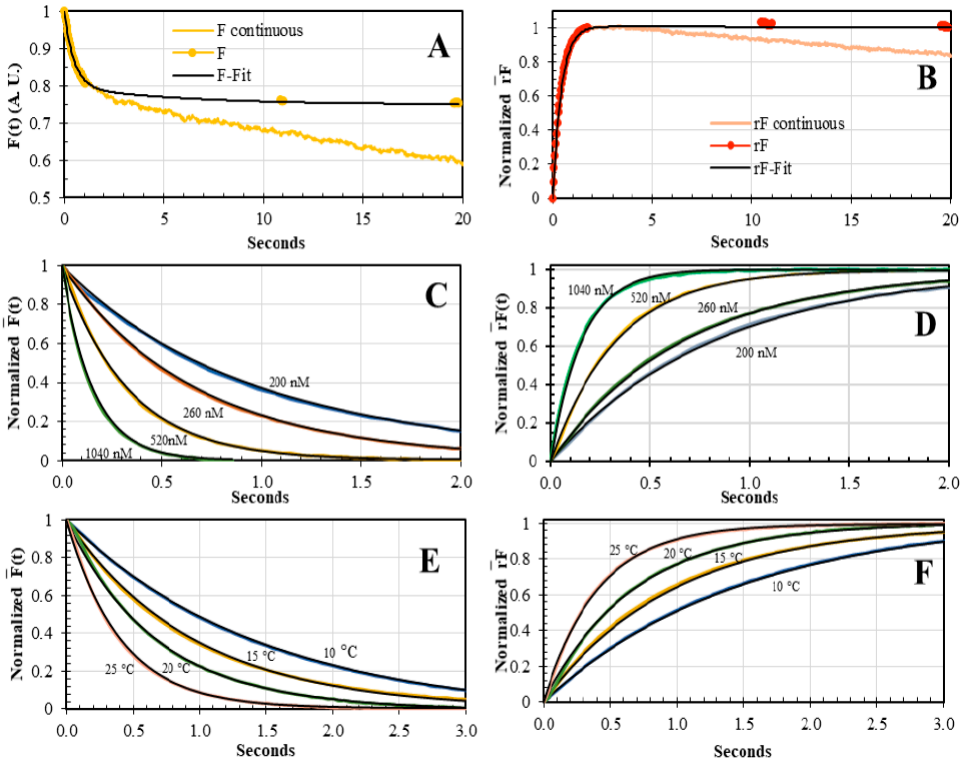

Figure 7. Concentration and temperature dependence of the AV-BcO association kinetics. (**A**,**B**) The *F(t)* and $\overline{rF}(t)$ sensing modalities were collected with the dual-channel SF under continuous (pale line) and discontinuous (dotted line) laser excitation at 488 nm. The *F(t)* trace, under continuous excitation, showed a second eigenvalue (λ_2) that ranged from 0.02 s^{-1} to 0.01 s^{-1} caused by photobleaching. In contrast, when the excitation was blocked, the intensity stayed constant after the reaction was completed, so that, the intensity decreased by 25.3 ± 2.2% and it was proportional to a change in the *QY* of 0.91 ± 0.01 for the free BcO probe and the 0.68 ± 0.02 of the AV-BcO complex (Table 2). (**C**,**D**) The concentration-dependence of the binding reaction of BcO (20 nM) and AV (200 nM, 260 nM, 520 nM and 1040 nM), at 20 °C, for both $\overline{F}(t)$ and $\overline{rF}(t)$ sensing modalities, respectively. (**E**,**F**) The temperature-dependence in the binding reactions of BcO (20 nM) and AV (260 nM) at 10 °C, 15 °C, 20 °C and 25 °C, were tracked by $\overline{F}(t)$ and $\overline{rF}(t)$ modalities. The black lines corresponded to the fitted curves that yielded the λ and k_{on} values, shown in Table 4.

On the other hand, the Δ*F(t)* dropped by 25% and produced a small distortion in the *r(t)* traces; therefore, the *r(t)* needed to be analyzed as *rF(t)*, as shown in Equation (15) [17]. As the AV-BcO complex is formed, the rotation of the probe decreased as shown by the $\overline{rF}(t)$ traces, which were collected only by two SF methodologies: polarizers and dual-channel SF (Figure 6F,H). The $\overline{rF}(t)$ traces acquired by these methodologies yielded equivalent eigenvalues, which were also in perfect agreement with the information obtained by the $\overline{F}(t)$ sensing modality. Thus, $\overline{F}(t)$ and $\overline{rF}(t)$ traces yielded k_{on} overlapping values, which indeed validated the accuracy of the dual-channel SF methodology (Table 3, Figure 6).

3.3. Concentration and Temperature Dependence of AV-BcO Binding Association Acquired by Dual-Channel SF

After validation of the dual-channel methodology, we acquired the AV-BcO traces as a function of concentration and temperature. For the former case, the $\overline{F}(t)$ and $\overline{rF}(t)$ sensing modalities showed an increment in the reaction velocity when the protein concentration increased from 200 nM, 260 nM, 520 nM up to 1040 nM, for all the temperatures tested, from 10 °C to 25 °C. Consequently, when the concentration increased, the resulted fits yielded increasing λ values that were equivalent to both sensing modalities (Figure 7, Table 4). For instance, for the $\overline{F}(t)$ traces at 20 °C, the $t_{1/2}$ were

584 ms ± 21 ms, 465 ms ± 8 ms, 228 ms ± 6 ms, and 112 ms ± 10 ms, and for the $\overline{rF}(t)$ traces, the $t_{1/2}$ were 586 ms ± 11 ms, 449 ms ± 9 ms, 229 ms ± 2 ms, and 109 ms ± 1 ms, respectively. The λ values of $\overline{F}(t)$ and $\overline{rF}(t)$ traces at each concentration, resulted in k_{on} values equivalent for both sensing modalities (Table 4).

The AV-BcO reaction speed also showed a temperature dependence from 10 °C to 25 °C from both $\overline{F}(t)$ and $\overline{rF}(t)$ sensing modalities. Thus, for the former traces, the $t_{1/2}$ values were 1,102.0 ms ± 0.074 ms, 655 ms ± 0.010 ms, 465 ms ± 0.008 ms and 0.281 ms ± 0.002 s from 10 °C, 15 °C, 20 °C, and 25 °C. These $t_{1/2}$ overlapped within the error of the $\overline{rF}(t)$ values of 1004.0 ms ± 0.050 ms, 670 ms ± 0.003 ms, 449 ms ± 0.004 ms and 0.280 ms ± 0.002 s, for the same order of the listed temperatures (Figure 7C,D). The k_{on} values increased 47.9 % from 10 °C to 15 °C, 53.9 % from 15 °C to 20 °C, and 60.9 % from 20 °C to 25 °C, suggesting a strong temperature dependence in good accordance with ITC titrations [44].

3.4. The yTBP-AdMLP$_{14ds}$ Association Traces Acquired by Dual-Channel and FRET SF Methodologies

To initiate gene transcription, the RNA polymerase II (RNAPII) needs the binding and bending of TBP to the TATA sequence (AdMLP) situated at the -31 nucleotide position of the first transcription codon [35]. Therefore, the yTBP-AdMLP complex formation is critical for gene expression [34] but it also requires several other proteins to form a multiprotein pre-initiation complex (PIC) to ensure the fidelity of transcription [32,36,39,45]. Here, we acquired the $\overline{F}(t)$ and $\overline{r}(t)$ traces of the yTBP (Figure 8, Figure S1) binding to the single labeled AdMLP$_{14ds}$ probes labeled with tethered Ta, Xr, and Fl dyes and contrasted with $F(t)_{FRET}$ traces acquired with the double-labeled Xr*AdMLP$_{14ds}$*Fl probe.

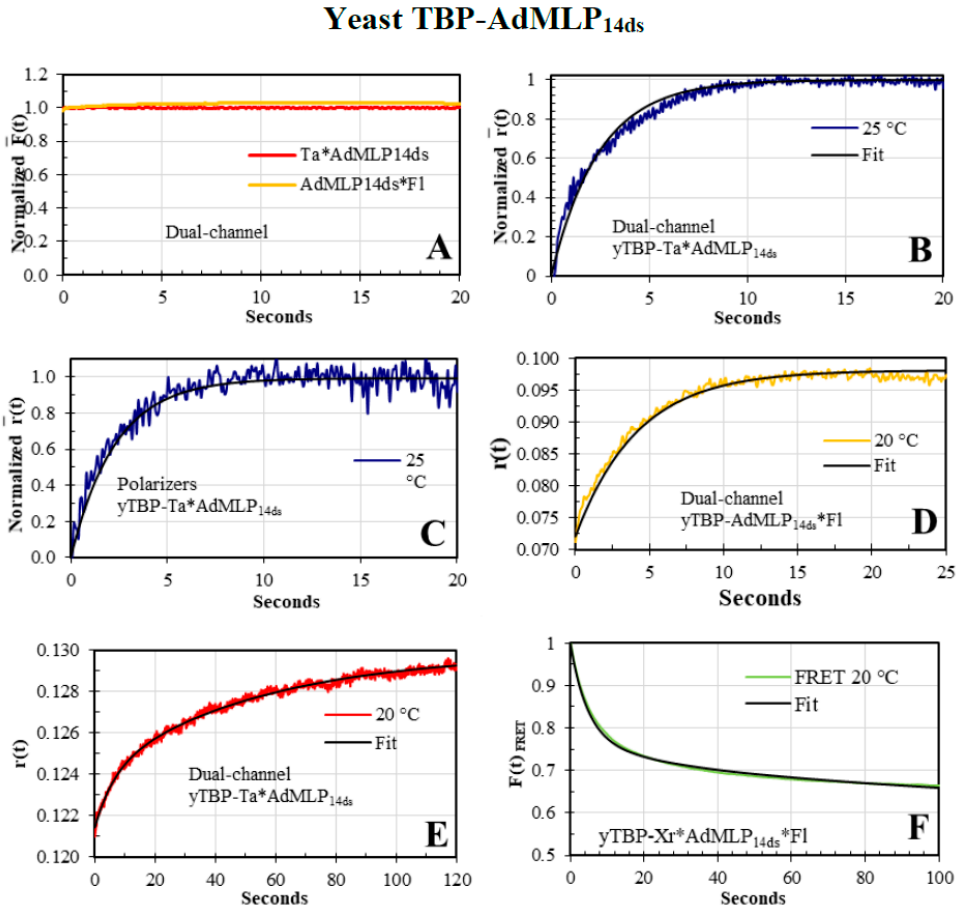

Figure 8. Yeast TBP-AdMLP$_{14ds}$ association kinetics. (**A**) The dual-channel $\overline{F}(t)$ traces of yTBP (500 nM)-Ta*AdMLP$_{14ds}$ (40 nM, red), and yTBP (420 nM)-AdMLP$_{14ds}$*Fl (40 nM, orange line) were not sensible to the binding process; in contrast, the *r(t)* traces were sensible to the complex formation. (**B**,**C**) The $\overline{r}(t)$ association reaction of yTBP (500 nM)-Ta*AdMLP$_{14ds}$ (40 nM), at 25 °C, were acquired

by the dual-channel and polarizer SF methodologies whose fitted traces (black line) were mono-exponentials, $1 - \alpha \times e(-\lambda \times t)$, with λ= 0.384 s^{-1} (±0.020 s^{-1}) and λ= 0.436 s^{-1} (±0.035 s^{-1}), respectively. The dual-channel and polarizer *r(t)* traces resulted in k_{on} values of 1.54 (±0.08) × 10^6 $M^{-1}s^{-1}$ and 1.74 (±0.14) × 10^6 $M^{-1}s^{-1}$, respectively; and were in the error range of first rate constant (k_{+1}) of 1.59 [0.03−0.07] × 10^6 $M^{-1}s^{-1}$, reported by FRET analysis, at 25 °C [11]. (**D**) At 20 °C, the *r(t)* dual-channel SF association reaction of yTBP (420 nM)-AdMLP$_{14ds}$*Fl (20 nM) was also mono-exponential (black line) with a λ= 0.247 s^{-1} (±0.025) s^{-1}, which yielded a k_{on} of 5.87 (±0.60) × 10^5 $M^{-1}s^{-1}$. (**E**) The 5′-Ta single labeled probe was used to acquire the *r(t)* dual-channel SF association reaction of yTBP (440 nM)-Ta*AdMLP$_{14ds}$ (40 nM), at 20 °C. The trace was fitted to a bi-exponential model (black line) with the following parameters: α_1 = 97.39% (±0.20%), λ_1 = 0.1276 s^{-1} (±0.0256 s^{-1}), α_2 = 2.61% (±0.02)%, λ_2 = 0.0181 s^{-1} (±0.0200 $^{-1}$). The faster phase yielded in a k_{on} of 5.80 (± 1.16) × 10^5 $M^{-1}s^{-1}$ that is excellent agreement with the 5.80 (± 0.26) × 10^5 $M^{-1}s^{-1}$ reported, at 20 °C [11]. (**F**) The FRET SF association reaction of yTBP (220 nM)-Xr*AdMLP$_{14ds}$*Fl (20 nM), at 20 °C, showed a triphasic exponential-decay model: α_1 = 30.9% (±0.5%), λ_1 = 0.22 s^{-1} (± 0.01 s^{-1}), α_2 = 11.9% (±2.1%), λ_2 = 0.040 s^{-1} (±0.013 s^{-1}) and α_3 = 58.2% (±0.9%), λ_3 = 0.0012 s^{-1} (±0.0002 s^{-1}). The fast λ_1 yielded a k_{on}= 5.50 (±0.25) × 10^5 $M^{-1}s^{-1}$ which is in excellent agreement with the k_{+1}= 5.80 (±0.26) × 10^5 $M^{-1}s^{-1}$ reported at 20 °C [11].

The $\overline{F}(t)$ traces of yTBP binding to the Ta*AdMLP$_{14ds}$ and AdMLP$_{14ds}$*Fl probes did not show any fluorescence change (Figure 8A). On the other hand, the $\overline{r}(t)$ sensing modality tracked very well the binding process (Figure 8B,C); therefore, the association kinetic can be studied with the $\overline{r}(t)$ traces and there is no need to obtain the $\overline{rF}(t)$ product as in the AV-BcO case (Figures 6 and 7). To ensure that dual-channel traces were reliable for the yTBP-Ta*AdMLP$_{14ds}$ complex formation, we compared them with the traces acquired by the polarizer methodology, at 25 °C (Figure 8B,C). Indeed, both methodologies yielded traces that resulted in overlapping λ values in the error (Figure 8B,C) that yielded the initial rate constant (k_{+1}), at 25 °C, of the complex reaction mechanism previously elucidated by $F(t)_{FRET}$, which consisted of six rate constants for a two-intermediates reaction [11].

To further evaluate the dual-channel *r(t)* traces, we compared yTBP binding, at 20 °C, with the single labeled AdMLP$_{14ds}$*Fl (Figure 8D), Xr*AdMLP$_{14ds}$ (Figure 8E), and the FRET Xr*AdMLP$_{14ds}$*Fl probe (Figure 8F), at the same protein/probe ratio. The $\Delta F(t)_{FRET}$ traces dropped 34.0% ± 2.0% (Equation (15)) for the yTBP-Xr*AdMLP$_{14ds}$*Fl and the $F(t)_{FRET}$ traces were described by three eigenvalues (λ_1, λ_2, and λ_3) whose faster component matched with the one observed with the *r(t)* traces (Figure 8D,E). The *r(t)* traces of yTBP-AdMLP$_{14ds}$*Fl and yTBP-Ta*AdMLP$_{14ds}$, at 20 °C, yielded k_{on} values that overlapped in error between each other and as well with the k_{+1} acquired in this study by $F(t)_{FRET}$ and elsewhere [11]. To analyze conformational changes, we acquired the time-resolved FRET (trFRET) of the free single labeled AdMLP$_{14ds}$*Fl and bound to yTBP and cTBP. We also obtained trFRET of the unbound double-labeled Xr*AdMLP$_{14ds}$*Fl and Ta*AdMLP$_{14ds}$*Fl, and the respective yTBP and cTBP complex (Table 5) to obtain the $\overline{R}$ and σ parameters for free duplexes and complexes (Figure 9A,B). The trFRET lifetime in ns, $\Sigma\alpha_i\tau_i$ or $\tau_{D(A)}$, of the free and yTBP bound probe, Xr*AdMLP$_{14ds}$*Fl and yTBP-Xr*AdMLP$_{14ds}$*Fl were 1.575 ns ± 0.066 ns and 1.042 ns ± 0.040 ns, respectively. The $\Delta t_{D(A)}$ between the free Xr*AdMLP$_{14ds}$*Fl and bound to the yTBP-Xr*AdMLP$_{14ds}$*Fl complex was 33.8% ± 2.0 % and it was equivalent to the observed $\Delta F(t)_{FRET}$ in the association traces. Likewise, the $\Delta t_{D(A)}$ when Ta was used as acceptor was 33.5% ± 1.7% (Table 5). The bend angles α were equivalent for both yTBP-Ta*AdMLP$_{14ds}$*Fl and yTBP-Xr*AdMLP$_{14ds}$*Fl complexes with values of 79.8° and 79.2°, respectively (Figure 9C).

Table 5. Time-resolved FRET of the free duplexes and TBP bound to $AdMLP_{14ds}$*Fl, Xr*$AdMLP_{14ds}$*Fl, and Ta*$AdMLP_{14ds}$*Fl, at 20 °C. All the decays were best described by a bi-exponential decay model according to the statistical parameters χ^2, Durbin-Watson (*DW*), and *Z* run (Equation (21)).

Sample	χ	*DW*	*Z*	α	τ *(ns)*	α	τ *(ns)*	φ *(ns)* [a]	φ *(ns)*	$\alpha_i\tau_i$ *(ns)* [b]
$AdMLP_{14ds}$*Fl	0.985 ± 0.030	1.965 ± 0.135	0.069 ± 0.400	0.340 ± 0.033	0.852 ± 0.098	0.660 ± 0.033	3.729 ± 0.043	0.105 ± 0.012	0.895 ± 0.012	2.749 ± 0.132
Xr*$AdMLP_{14ds}$*Fl	1.008 ± 0.030	2.027 ± 0.115	−0.075 ± 0.352	0.494 ± 0.033	0.645 ± 0.097	0.506 ± 0.033	2.493 ± 0.119	0.201 ± 0.022	0.799 ± 0.022	1.575 ± 0.066
Ta*$AdMLP_{14ds}$*Fl	0.984 ± 0.040	1.942 ± 0.067	−0.021 ± 0.170	0.520 ± 0.014	0.607 ± 0.034	0.480 ± 0.014	2.230 ± 0.037	0.279 ± 0.049	0.949 ± 0.173	1.385 ± 0.042
cTBP-$AdMLP_{14ds}$*Fl	1.009 ± 0.022	1.987 ± 0.132	−0.006 ± 0.404	0.315 ± 0.013	0.826 ± 0.123	0.685 ± 0.013	3.823 ± 0.084	0.090 ± 0.012	0.910 ± 0.012	2.878 ± 0.096
yTBP-$AdMLP_{14ds}$*Fl	1.016 ± 0.029	1.916 ± 0.086	−0.050 ± 0.349	0.330 ± 0.018	0.852 ± 0.060	0.670 ± 0.018	3.998 ± 0.127	0.095 ± 0.005	0.905 ± 0.005	2.959 ± 0.149
cTBP-Xr*$AdMLP_{14ds}$*Fl	1.018 ± 0.026	2.017 ± 0.157	0.160 ± 0.313	0.715 ± 0.036	0.428 ± 0.043	0.285 ± 0.036	1.763 ± 0.112	0.381 ± 0.048	0.619 ± 0.048	0.805 ± 0.034
yTBP-Xr*$AdMLP_{14ds}$*Fl	1.016 ± 0.010	1.916 ± 0.045	−0.185 ± 0.114	0.668 ± 0.013	0.529 ± 0.035	0.332 ± 0.013	2.077 ± 0.047	0.339 ± 0.010	0.661 ± 0.010	1.042 ± 0.040
cTBP-Ta*$AdMLP_{14ds}$*Fl	1.011 ± 0.024	1.972 ± 0.142	0.388 ± 0.234	0.772 ± 0.012	0.434 ± 0.010	0.228 ± 0.012	1.601 ± 0.022	0.335 ± 0.010	0.364 ± 0.014	0.699 ± 0.010
yTBP-Ta*$AdMLP_{14ds}$*Fl	0.974 ± 0.058	1.902 ± 0.106	0.299 ± 0.344	0.806 ± 0.008	0.564 ± 0.032	0.194 ± 0.008	2.264 ± 0.068	0.509 ± 0.007	0.491 ± 0.007	0.894 ± 0.046

[a] The φ parameters are the normalized contribution of each phase in nanoseconds (ns). [b] The area under the deconvoluted decay is described by $\Sigma\alpha_i\tau_i$.

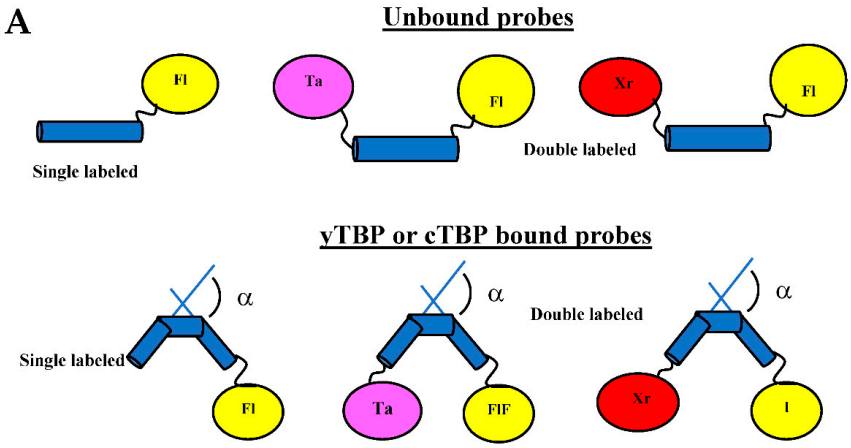

B

Sample	$\overline{R}$ (Å)	σ (Å)
Ta*AdMLP$_{14ds}$*Fl	62.8	5.2
yTBP-Ta*AdMLP$_{14ds}$*Fl	52.4	8.7
cTBP-Ta*AdMLP$_{14ds}$*Fl	49.9	7.0
Xr*AdMLP$_{14ds}$*Fl	65.6	5.7
yTBP-Xr*AdMLP$_{14ds}$*Fl	55.2	7.4
cTBP-Xr*AdMLP$_{14ds}$*Fl	51.0	6.9

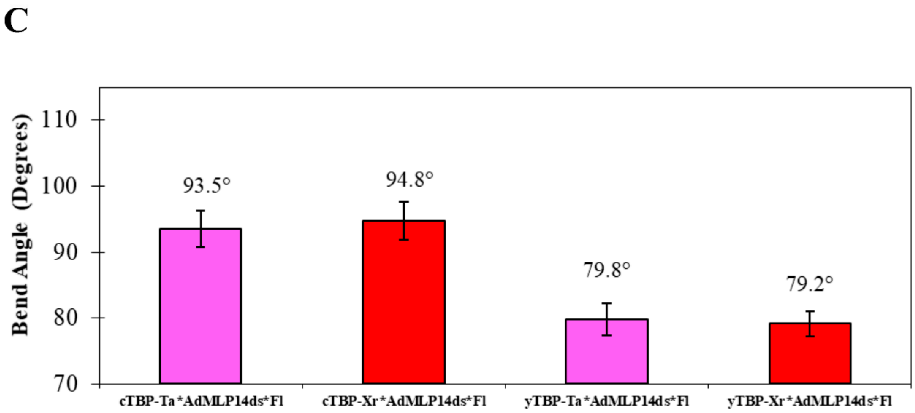

Figure 9. The interdye distances and bend angles of free AdMLP$_{14ds}$ probes and bound to cTBP and yTBP, at 20 °C. (**A**) To calculate the *P(R)* distance distribution, it is required to obtain the lifetime of the single and double-labeled probe as free and bound complexes with TBP proteins. The Xr*AdMLP$_{14ds}$*Fl and Ta*AdMLP$_{14ds}$*Fl probes were straight but after complex formation with yTBP or cTBP, the DNA is bent, which shortens the interdye $\overline{R}$ resulting in more energy transfer from Fl donor toward the acceptor (Ta or Xr). (**B**) The *P(R)* distance distribution is described by the mean distance $\overline{R}$ and the spread σ of the unbound probes and the respective complexes formed with yTBP and cTBP. (**C**) The bend angle (α) of the TATA distortion for the canonical AdMLP is calculated according to Equation (25), requiring the $\overline{R}$-value and where *L2* was 20.4 Å. The bend angle produced by each protein was independent of the probe used since the values overlapped in error for the Xr*AdMLP$_{14ds}$*Fl and Ta*AdML$_{P14ds}$*Fl complexes formed with yTBP and cTBP, respectively. The bend angles caused by cTBP for both probes were larger than those observed by yTBP since the latter has an N-terminal domain that regulated the binding and shifts the equilibrium to the left, or towards the reactants [40].

3.5. Core TBP-AdMLP$_{14ds}$ Association Kinetics Acquired by Dual-Channel and FRET SF Methodologies

We also contrasted the $\overline{r}(t)$ dual-channel association trace of cTBP and AdMLP acquired with the single labeled Xr*AdMLP$_{14ds}$ probe (Figure 10A, purple line, Figure S1) and the $F(t)_{FRET}$ trace collected with the double-labeled Xr*AdMLP$_{14ds}$*Fl probe (Figure 10A, yellow line). The association reaction reactions were collected under discontinuous excitation to eliminate the photobleaching effect and the respective fit passed through the traces (solid and slashed lines, Figure 10A). The cTBP has the N-terminal domain truncated in comparison with the full-length yTBP and as previously described for full-length yTBP-AdMLP, the $\overline{F}(t)$ trace of cTBP-Xr*AdMLP$_{14ds}$*Fl was not sensitive to the protein binding but the $\overline{r}(t)$ trace tracked the complex formation by increasing its value as the dye rotation decreased. For the FRET probe, the $\overline{F}(t)_{FRET}$ trace decreased as the cTBP bent the probe, resulting in a decrement in the fluorescence by energy transfer. To visualize the comparison of these two traces, we inverted the $\overline{r}(t)$ trace and yielded just over the $\overline{F}(t)_{FRET}$ whose fitting lines overlap perfectly (Figure 10B).

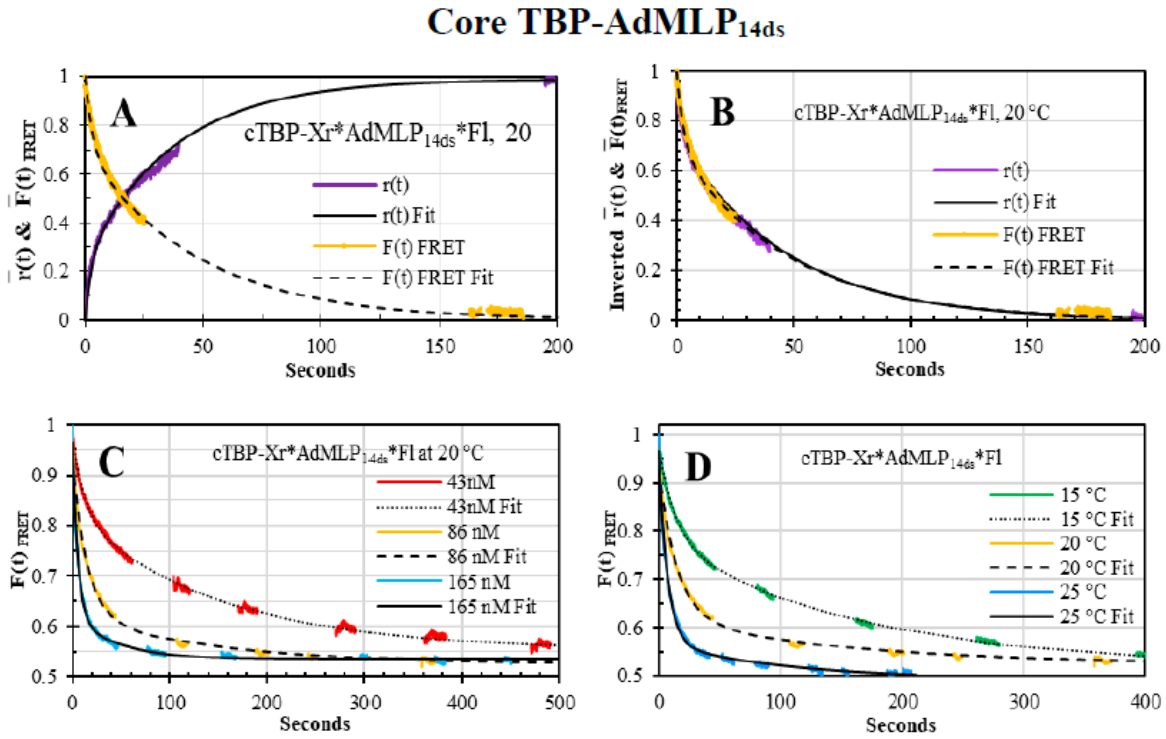

Figure 10. Core TBP-AdMLP$_{14ds}$ association kinetics. (**A**,**B**) The association kinetics of cTBP (260 nM)-Xr*AdMLP$_{14ds}$ (60 nM) and cTBP (86 nM)-Xr*AdMLP$_{14ds}$*Fl (20 nM) were monitored by $\overline{r}(t)$ (orange) and $\overline{F}(t)_{FRET}$ (purple) sensing modalities, at 20 °C. The $\overline{r}(t)$ and $\overline{F}(t)_{FRET}$ fits yielded eigenvalues of 0.350 (±0.040) s^{-1} and 0.337 (±0.078) s^{-1}, which resulted in k_{on} values of 1.35 (±0.05) × 10^6 $M^{-1}s^{-1}$ and 1.30 (± 0.10) × 10^6 $M^{-1}s^{-1}$, respectively. Both k_{on} values are in excellent agreement since the protein/probe ratio is 4.3 and they are in the error range of the reported k_{+1} of 1.26 (±0.05) × 10^6 $M^{-1}s^{-1}$, at 25 °C [2]. (**C**) The concentration dependence of the cTBP-AdMLP$_{14ds}$ complex was observed by the $\overline{F}(t)_{FRET}$ sensing modality with cTBP at 43 nM (red), 86 nM (orange), and 165 nM (blue) concentrations, at 20 °C, reacting with 20 nM Xr*AdMLP$_{14ds}$*Fl. (**D**) The temperature dependence was also monitored by the $\overline{F}(t)_{FRET}$ traces, at 15 °C (green), 20 °C (orange), and 25 °C (blue) of 86 nM cTBP reacting with 20 nM Xr*AdMLP$_{14ds}$*Fl. The FRET global fits (black lines) of the concentration and temperature dependence traces yielded a two-intermediate reaction mechanism with k_{+1} values of 9.62 (±0.41) × 10^5 $M^{-1}s^{-1}$, 1.26 (±0.05) × 10^6 $M^{-1}s^{-1}$ and 1.64 (±0.06) × 10^6 $M^{-1}s^{-1}$ at 15 °C, 20 °C and 25 °C, respectively [2].

The $F(t)_{FRET}$ traces of the cTBP-AdMLP reactions showed concentration dependence when the protein concentration increased from 43 nM, 86 nM, and 165 nM (Figure 10 C) while the concentration of Xr*AdMLP$_{14ds}$*Fl, was constant at 20 nM, at 20 °C. Furthermore, there was a temperature dependence as the reaction speed increased from 15 °C, up to 25 °C, at 86 nM cTBP and 20 nM Xr*AdMLP$_{14ds}$*Fl (Figure 10D). These observed reactions were completed at 49.0% ± 1.0% whose fits showed three exponential phases (black lines). In addition, we measured the trFRET lifetimes of the unbound Xr*AdMLP$_{14ds}$*Fl and Ta*AdMLP$_{14ds}$*Fl and complexed by cTBP (Table 5) whose corresponding changes were 48.9% ± 3.0% and 49.5% ± 2.0%, respectively, perfectly matching the $F(t)_{FRET}$ association change. The $\overline{R}$ and σ were obtained for the free probes Xr*AdMLP$_{14ds}$*Fl and Ta*AdMLP$_{14ds}$*Fl and the respective complexes formed by the cTBP (Figure 9B). The cTBP bend angle was larger than α produced by the full-length yTBP (Figure 9C) since the N-terminal domain has a regulatory activity [2]. Both protein complexes formed with Xr*AdMLP$_{14ds}$*Fl and Ta*AdMLP$_{14ds}$*Fl yielded equivalent bend angles showing that acceptor Ta and Xr dyes are excellent FRET biosensors and yielded the same results.

3.6. Ternary Association Kinetics of TFIIA and the Binary yTBP-AdMLP$_{31ds}$ Acquired by Dual-Channel SF

The function of TFIIA in the PIC complex is to shift the equilibrium towards a rearranged more stable state, as shown by 3D cryo-EM reconstructions [54]. To test out the dual-channel SF ability to measure large complexes, we used a longer 31mer internally-labeled with fluorescein (AdMLP$_{31ds}$*Fl$_{int}$) to allow space for the TFIIA binding at the 5′ upstream of the TATA sequence [39,41,55]. First, we validated the yTBP binding to the longer AdMLP$_{31ds}$*Fl$_{int}$, and in contrast to the 3′Fl in the shorter AdMLP$_{14ds}$ probes, the Fl$_{int}$ was sensitive to yTBP binding since the *QY* dropped 15.5% (Table 2), and consequently the binding was followed as well by the *F(t)* sensing modality (Figure 11A). Interestingly, the *QY* increased after TFIIA binding (Table 2). To compensate for *QY* changes, the *r(t)* was multiplied by *F(t)* to analyze the $\overline{rF}(t)$ sensing modality, at 20 °C and 30 °C (Figure 11B), thus the resulting k_{on} overlapped with the reported k_{+1} values at the same temperatures indicating that longer probe is functional [11] and in excellent accord with the shorter single labeled and double-labeled probes (Figure 8).

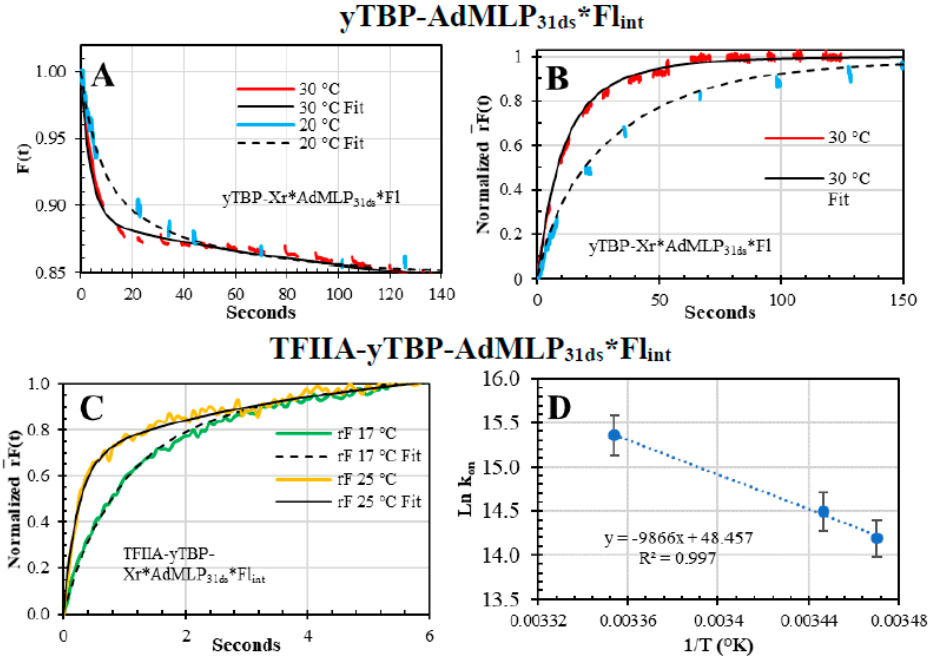

Figure 11. Association kinetic of binary yTBP-AdMLP$_{31ds}$*Fl$_{int}$ and ternary complex TFIIA-yTBP-AdMLP$_{31ds}$*Fl$_{int}$. (**A**) The association traces of yTBP (220 nM) and AdMLP$_{31ds}$*Fl$_{int}$ (20 nM), at 20 °C (blue) and 30 °C (red), were monitored by the *F(t)* sensing modality, yielding parameters of α_1 = 8.0% (±1.0%),

λ_1 = 0.15 s^{-1} (±0.010 s^{-1}), α_2 = 7.0% (±1.0%), λ_2 = 0.025 s^{-1} (±0.010 s^{-1}), baseline = 85.0% ± 2.0%; and α_1 = 9.8% (±0.3%), λ_1 = 0.26 s^{-1} (±0.03 s^{-1}), α_2 = 5.2% (±0.3%), λ_2 = 0.0085 s^{-1} (±0.0015 s^{-1}), baseline = 85.0% ± 2.0%, respectively. (**B**) The $\overline{rF}(t)$ association traces of binary yTBP (220 nM)-AdMLP$_{31ds}$*Fl$_{int}$ (20 nM) complex, at 20 °C, yielded the following parameters: α_1 = 27.2% (±11.6%), λ_1= 0.1245 s^{-1} (±0.0133) s^{-1}, α_2 = 72.8% (±6.1)%, λ_2 = 0.0221 s^{-1} (±0.0060 s^{-1}); and at 30 °C, the parameters were: α_1 = 35.0% (±8.0)%, λ_1 = 0.30 s^{-1} (±0.03 s^{-1}), α_2 = 65.0% (±7.0%), λ_2 = 0.925 s^{-1} (±0.06 s^{-1}). The k_{on} values for this longer probe in the yTBP-AdMLP31ds*Fl$_{int}$, at 20 °C and 30 °C, were calculated with the faster λ_1 resulting in values of 5.91 (± 0.46) × 10^5 $M^{-1}s^{-1}$ and 4.20 (± 0.27) × 10^5 $M^{-1}s^{-1}$, respectively, which were in excellent agreement with the respective values of 5.80 (± 0.26) × 10^5 $M^{-1}s^{-1}$ and 4.21 (± 0.19) × 10^5 $M^{-1}s^{-1}$, obtained with the 14-nucleotide probe (yTBP-AdMLP$_{14ds}$*Fl), at the same temperatures, respectively [11]. (**C**) The dual-channel-SF association of yTFIIA (850 nM) and the binary yTBP (220 nM)-AdMLP$_{31ds}$*Fl$_{int}$ (20 nM) complex, at 15 °C (blue), 17 °C (green), and 25 °C (orange), were biphasic with normalized values of α_1 = 55.5% (±9.0%), λ_1 = 1.24 s^{-1} (±0.33 s^{-1}), α_2 = 44.5% (±15.0%), λ_2 = 0.18 s^{-1} (±0.05 s^{-1}); α_1 = 53.7% (±8.5%), λ_1 = 1.56 s^{-1} (±0.33 s^{-1}), α_2 = 39.5 % (±12.7%), λ_2 = 0.20 s^{-1} (±0.06 s^{-1}); and α_1 = 63.4% (±0.06%), λ_1 = 3.98 s^{-1} (±1.35 s^{-1}), α_2 = 32.6% (±7.6%), λ_2 = 0.24 s^{-1} (±0.01 s^{-1}), respectively. The calculated k_{on} values, at 15 °C, 17 °C and 25 °C, were 1.45 (±0.3) × 10^6 $M^{-1}s^{-1}$, 1.84 (±0.34) × 10^6 $M^{-1}s^{-1}$ and 4.68 (±1.59) × 10^6 $M^{-1}s^{-1}$, respectively. (**D**) The calculated van't Hoff plot yielded an enthalpy of 19.6 ± 1.6 Kcal/mol for the yTFIIA and yTBP-AdMLP$_{31ds}$*Fl$_{int}$ binding process.

After confirming that the longer probe is functional, we pre-formed the binary yTBP-AdMLP$_{31ds}$*Fl$_{int}$ complex and reacted with TFIIA, at 15 °C, 17 °C, and 25 °C, which was tracked by the *rF(t)* sensing modality (Figure 11C). The k_{on} values of TFIIA binding to the binary complex, at 15 °C 17 C, and 25 °C, were 1.45 (±0.3) × 10^6 $M^{-1}s^{-1}$ and 4.68 (±1.59) × 10^6 $M^{-1}s^{-1}$. There is a reported dissociation rate constant of the ternary TFIIA-TBP-TATA of 7.1 × 10^{-4} s^{-1} at room temperature [38], which let us estimate the K_D values between 2.1 nM and 6.6 nM for yTFIIA and the binary yTBP-TATA complex, between the 15 °C and 25 °C range.

4. Conclusions

We evaluated the electronic filters and custom-tailored instrument control system of a new dual-channel SF apparatus that allows simultaneous acquisition of the *F(t)* and *r(t)* with an optical train in L-type configuration [18,19]. In our dual-channel SF apparatus, we economized by a factor of two the biomolecule solution consumption in comparison to the polarizer SF, allowing us to preserve precious labeled biological material such as proteins, DNA, RNA, ligands, and other labeled biomolecules [19]. To validate our dual-channel SF, we tracked multiple association reactions at diverse conditions and contrasted the resulted k_{on} values with those acquired by other methodologies with multiple sensing modalities, such as *r(t)*, *F(t)*, *rF(t)*, and $F(t)_{FRET}$.

In conclusion, the dual-channel SF has functional and robust electronic filtering since the tested circuit separates the V_{DC} and V_{AC} signals and stores them in separate spreadsheets, acquiring the *r(t)* and *F(t)* information in one single shot. The calculated k_{on} values acquired by the dual-channel SF traces showed ~50% lower noise levels, as shown in the errors reported in Table 3. Our new setting was reliable and allowed the association traces of relevant biological complexes by monitoring the *F(t)*, *r(t)*, and *rF(t)* sensing modalities. Our work describes new hardware to collect kinetic data at different concentrations and temperatures to elucidate reaction mechanisms [56] and thermodynamic information according to the Arrhenius equation [57,58] and Eyring relationship [59,60], which is relevant for protein-protein, protein-DNA, or protein-drug studies [61,62].

Supplementary Materials: The following are available online at http://www.mdpi.com/2079-6374/10/11/180/s1, Figure S1. The grating-factor of the fluorimeter and the stopped-flow.

Author Contributions: Conceptualization, R.F.D. and L.J.P.; methodology, R.F.D.; software, R.F.D.; validation, R.F.D., L.J.P., K.Z.-R., N.V.-V., and K.A.C.; formal analysis, R.F.D.; investigation, R.F.D.; resources, R.F.D.; data curation, R.F.D.; writing—original draft preparation, R.F.D.; writing—review and editing, R.F.D., K.Z.-R., O.O., N.V.-V.,

and K.A.C.; visualization, R.F.D.; supervision, R.F.D. and L.J.P.; project administration, R.F.D. and L.J.P.; funding acquisition, R.F.D., L.J.P., and O.O. All authors have read and agreed to the published version of the manuscript.

Funding: This research was funded by the National Institutes of Health Grants GM59346 and RR015468 to L.J.P.; CONACYT-Mexico postdoctoral and SNI fellowships (130994, 162809, SNI75487).

Acknowledgments: We thank Efrain Soto-Apolinar for reviewing the mathematical equations and Blas Rodriguez for helping in the matrix analysis. Roberto F. Delgadillo thanks Carolina Flores-Ballesteros and Alethia D. Guzman for proofreading the manuscript, and he would like to thank the Department of Engineering and Science, North Region, of the Tecnológico de Monterrey for the support given, CONACYT-Mexico for the postdoctoral fellowships, the "Sistema Nacional de Investigadores" (SNI-CONACYT) fellowship, and the Government of Veracruz-Mexico.

Conflicts of Interest: The author K.A.C. is an employee of GlaxoSmithKline, which provided support in the form of salary for her but did not have any additional role in the study design, data collection, and analysis, decision to publish, or preparation of the manuscript. The specific roles of these authors are articulated in the 'author contributions' section. The authors have no further competing interests to declare. The funders had no role in the design of the study; in the collection, analyses, or interpretation of data; in the writing of the manuscript, or in the decision to publish the results.

References

1. Goss, D.J.; Parkhurst, L.J.; Wahba, A.J. Kinetic studies of the rates and mechanism of assembly of the protein synthesis initiation complex. *Biophys. J.* **1980**, *32*, 283–293. [CrossRef]
2. Delgadillo, R.F.; Whittington, J.D.E.; Parkhurst, L.K.; Parkhurst, L.J. The TATA-Binding Protein Core Domain in Solution Variably Bends TATA Sequences via a Three-Step Binding Mechanism. *Biochemistry* **2009**, *48*, 1801–1809. [CrossRef] [PubMed]
3. Whittington, J.D.E.; Delgadillo, R.F.; Attebury, T.J.; Parkhurst, L.K.; Daugherty, M.A.; Parkhurst, L.J. TATA-Binding Protein Recognition and Bending of a Consensus Promoter Are Protein Species Dependent. *Biochemistry* **2008**, *47*, 7264–7273. [CrossRef] [PubMed]
4. Galletto, R.; Maillard, R.; Jezewska, M.J.; Bujalowski, W. Global Conformation of the Escherichia coli Replication Factor DnaC Protein in Absence and Presence of Nucleotide Cofactors. *Biochemistry* **2004**, *43*, 10988–11001. [CrossRef]
5. Hartridge, H.H.; Roughton, F.J.W. A method of measuring the velocity of very rapid chemical reactions. *Proc. R. Soc. Lond. Ser. A* **1923**, *104*, 376–394.
6. Chance, B. The accelerated flow method for rapid reactions. *J. Franklin Inst.* **1940**, *229*, 737–766. [CrossRef]
7. Gibson, Q.H. [6] Rapid mixing: Stopped flow. *Methods Enzymol.* **1969**, 187–228. [CrossRef]
8. Berger, R.L.; Balko, B.; Borcherdt, W.; Friauf, W. High Speed Optical Stopped-Flow Apparatus. *Rev. Sci. Instrum.* **1968**, *39*, 486–493. [CrossRef] [PubMed]
9. Trojanowicz, M. Flow Chemistry in Contemporary Chemical Sciences: A Real Variety of Its Applications. *Molecules* **2020**, *25*, 1434. [CrossRef]
10. Cantor, C.R.; Schimmel, P.R. *Techniques for the Study of Biological Structure and Function (Pt. 2)*; W.H. Freeman and Co.: Oxford, UK, 1980.
11. Parkhurst, K.M.; Richards, R.M.; Brenowitz, M.; Parkhurst, L.J. Intermediate species possessing bent DNA are present along the pathway to formation of a final TBP-TATA complex. *J. Mol. Biol.* **1999**, *289*, 1327–1341. [CrossRef] [PubMed]
12. Gaikwad, A.; Gómez-Hens, A.; Perez-Bendito, D. Use of stopped-flow fluorescence polarization immunoassay in drug determinations. *Anal. Chim. Acta* **1993**, *280*, 129–135. [CrossRef]
13. Gaikwad, A.; Gómez-Hens, A.; Perez-Bendito, D. Estimation of opiates in urine by stopped-flow fluorimmunoassay. *Fresenius J. Anal. Chem.* **1993**, *347*, 450–453. [CrossRef]
14. Pérez-Bendito, D.; Gómez-Hens, A.; Gaikwad, A. Direct stopped-flow fluorescence polarization immunoassay of abused drugs and their metabolites in urine. *Clin. Chem.* **1994**, *40*, 1489–1493. [CrossRef] [PubMed]
15. Sendra, B. Kinetic determination of atrazine in foods based on stopped-flow fluorescence polarization immunoassay. *Talanta* **1998**, *47*, 153–160. [CrossRef]
16. Lakowicz, J.R. Fluorescence Polarization. In *Principles of Fluorescence Spectroscopy*; Springer: Boston, MA, USA, 1983; pp. 111–112.
17. Otto, M.R.; Lillo, M.P.; Beechem, J.M. Resolution of multiphasic reactions by the combination of fluorescence total-intensity and anisotropy stopped-flow kinetic experiments. *Biophys. J.* **1994**, *67*, 2511–2521. [CrossRef]
18. Lakowicz, J.R. Fluorescence Anisotropy. In *Principles of Fluorescence Spectroscopy*; Springer: Boston, MA, USA, 1999; pp. 291–319. [CrossRef]

19. Lakowicz, J.R. Fluorescence Anisotropy. In *Principles of Fluorescence Spectroscopy*; Springer: Boston, MA, USA, 2006; pp. 353–382. [CrossRef]
20. Canet, D.; Doering, K.; Dobson, C.M.; Dupont, Y. High-Sensitivity Fluorescence Anisotropy Detection of Protein-Folding Events: Application to α-Lactalbumin. *Biophys. J.* **2001**, *80*, 1996–2003. [CrossRef]
21. Beechem, J.M.; Sherman, M.A.; Mas, M.T. Sequential Domain Unfolding in Phosphoglycerate Kinase: Fluorescence Intensity and Anisotropy Stopped-Flow Kinetics of Several Tryptophan Mutants. *Biochemistry* **1995**, *34*, 13943–13948. [CrossRef]
22. Tang, G.-Q.; Patel, S.S. Rapid Binding of T7 RNA Polymerase Is Followed by Simultaneous Bending and Opening of the Promoter DNA. *Biochemistry* **2006**, *45*, 4947–4956. [CrossRef] [PubMed]
23. Galletto, R.; Bujalowski, W. Kinetics of the *E. Coli* replication Factor DnaC Protein−Nucleotide Interactions. II. Fluorescence Anisotropy and Transient, Dynamic Quenching Stopped-Flow Studies of the Reaction Intermediates. *Biochemistry* **2002**, *41*, 8921–8934. [CrossRef]
24. Rousseau, D.L.; Staros, J.V.; Beechem, J.M. The interaction of epidermal growth factor with its receptor in A431 cell membranes: A stopped-flow fluorescence anisotropy study. *Biochemistry* **1995**, *34*, 14508–14518. [CrossRef]
25. Wilkinson, J.C.; Beechem, J.M.; Staros, J.V. A stopped-flow fluorescence anisotropy method for measuring hormone binding and dissociation kinetics with cell-surface receptors in living cells. *J. Recept. Signal Transduct.* **2002**, *22*, 357–371. [CrossRef] [PubMed]
26. Phillips, R.; Hunter, J.L.; Eccleston, J.F.; Webb, M.R. The Mechanism of Ras GTPase Activation by Neurofibromin. *Biochemistry* **2003**, *42*, 3956–3965. [CrossRef] [PubMed]
27. Bradrick, T.; Philippetis, A.; Georghiou, S. Stopped-flow fluorometric study of the interaction of melittin with phospholipid bilayers: Importance of the physical state of the bilayer and the acyl chain length. *Biophys. J.* **1995**, *69*, 1999–2010. [CrossRef]
28. Badoz, J.; Billardon, M.; Canit, J.C.; Russel, M.F. Sensitive devices to determine the state and degree of polarization of a light beam using a birefringence modulator. *J. Opt.* **1977**, *8*, 373–384. [CrossRef]
29. Wampler, J.E.; DeSa, R.J. Recording Polarization of Fluorescence Spectrometer—A Unique Application of Piezoelectric Birefringence Modulation. *Anal. Chem.* **1974**, *46*, 563–567. [CrossRef]
30. Giblin, D.E. *A Modular Instrument for the Measurement of Transient Circular Dichroism, Fluorescence Polarization and Emission Anisotropy*; University of Nebraska-Lincoln: Lincoln, NE, USA, 1978.
31. Kornberg, R.D. The molecular basis of eucaryotic transcription. *Cell Death Differ.* **2007**, *14*, 1989–1997. [CrossRef] [PubMed]
32. Haberle, V.; Stark, A. Eukaryotic core promoters and the functional basis of transcription initiation. *Nat. Rev. Mol. Cell Biol.* **2018**, *19*, 621–637. [CrossRef]
33. Delgadillo, R.F. *Acceptor Detected Fluorescence Resonance Energy Transfer for Measurement up to 250 A and Biophysical Studies on Core TATA Binding Protein-DNA Complex*; University of Nebraska-Lincoln: Lincoln, NE, USA, 2009; Available online: http://digitalcommons.unl.edu/dissertations/AAI3388957/ (accessed on 1 October 2020).
34. Matsui, T.; Segall, J.; A Weil, P.; Roeder, R.G. Multiple factors required for accurate initiation of transcription by purified RNA polymerase II. *J. Biol. Chem.* **1980**, *255*, 11992–11996.
35. Kramm, K.; Engel, C.; Grohmann, D. Transcription initiation factor TBP: Old friend new questions. *Biochem. Soc. Trans.* **2019**, *47*, 411–423. [CrossRef] [PubMed]
36. Sikorski, T.W.; Buratowski, S. The basal initiation machinery: Beyond the general transcription factors. *Curr. Opin. Cell Biol.* **2009**, *21*, 344–351. [CrossRef]
37. Liu, Q.; Gabriel, S.E.; Roinick, K.L.; Ward, R.D.; Arndt, K.M. Analysis of TFIIA Function In Vivo: Evidence for a Role in TATA-Binding Protein Recruitment and Gene-Specific Activation. *Mol. Cell. Biol.* **1999**, *19*, 8673–8685. [CrossRef]
38. Hieb, A.R.; Halsey, W.A.; Betterton, M.D.; Perkins, T.T.; Kugel, J.F.; Goodrich, J.A. TFIIA Changes the Conformation of the DNA in TBP/TATA Complexes and Increases their Kinetic Stability. *J. Mol. Biol.* **2007**, *372*, 619–632. [CrossRef]
39. Bhuiyan, T.; Timmers, H.M. Promoter Recognition: Putting TFIID on the Spot. *Trends Cell Biol.* **2019**, *29*, 752–763. [CrossRef] [PubMed]
40. Delgadillo, R.F.; Parkhurst, L.J. Spectroscopic Properties of Fluorescein and Rhodamine Dyes Attached to DNA. *Photochem. Photobiol.* **2010**, *86*, 261–272. [CrossRef]
41. Young, C.S.H. The Structure and Function of the Adenovirus Major Late Promoter. *Future Hiv-1 Ther.* **2003**, 213–249. [CrossRef]

42. Parkhurst, K.M.; Brenowitz, M.; Parkhurst, L.J. Simultaneous Binding and Bending of Promoter DNA by the TATA Binding Protein: Real Time Kinetic Measurements†. *Biochemistry* **1996**, *35*, 7459–7465. [CrossRef]
43. Livnah, O.; Bayer, E.A.; Wilchek, M.; Sussman, J.L. Three-dimensional structures of avidin and the avidin-biotin complex. *Proc. Natl. Acad. Sci. USA* **1993**, *90*, 5076–5080. [CrossRef]
44. Delgadillo, R.F.; Mueser, T.C.; Zaleta-Rivera, K.; Carnes, K.A.; González-Valdez, J.; Parkhurst, L.J. Detailed characterization of the solution kinetics and thermodynamics of biotin, biocytin and HABA binding to avidin and streptavidin. *PLoS ONE* **2019**, *14*, e0204194. [CrossRef] [PubMed]
45. Bleichenbacher, M.; Tan, S.; Richmond, T.J. Novel Interactions Between the Components of Human and Yeast TFIIA/TBP/DNA Complexes. *J. Mol. Biol.* **2003**, *332*, 783–793. [CrossRef]
46. Goerisch, H.; Goss, D.J.; Parkhurst, L.J. Kinetics of ribosome dissociation and subunit association studied in a light-scattering stopped-flow apparatus. *Biochemistry* **1976**, *15*, 5743–5753. [CrossRef] [PubMed]
47. Arteaga, O.; Nichols, S.M.; Kahr, B. Mueller matrices in fluorescence scattering. *Opt. Lett.* **2012**, *37*, 2835–2837. [CrossRef]
48. Fisz, J. Another Look at Magic-Angle-Detected Fluorescence and Emission Anisotropy Decays in Fluorescence Microscopy. *J. Phys. Chem. A* **2007**, *111*, 12867–12870. [CrossRef]
49. Parkhurst, L.J.; Parkhurst, K.M.; Powell, R.; Wu, J.; Williams, S. Time-resolved fluorescence resonance energy transfer studies of DNA bending in double-stranded oligonucleotides and in DNA-protein complexes. *Biochemistry* **2002**, *61*, 180–200. [CrossRef]
50. Wu, J.; Parkhurst, K.M.; Powell, R.M.; Parkhurst, L.J. DNA Sequence-dependent Differences in TATA-binding Protein-induced DNA Bending in Solution Are Highly Sensitive to Osmolytes. *J. Biol. Chem.* **2001**, *276*, 14623–14627. [CrossRef]
51. Marquardt, D.W. An Algorithm for Least-Squares Estimation of Nonlinear Parameters. *J. Soc. Ind. Appl. Math.* **1963**, *11*, 431–441. [CrossRef]
52. Durbin, J.; Watson, G.S. Testing for Serial Correlation in Least Squares Regression. II. *Biometrika* **1951**, *38*, 159. [CrossRef] [PubMed]
53. Swed, F.S.; Eisenhart, C. Tables for Testing Randomness of Grouping in a Sequence of Alternatives. *Ann. Math. Stat.* **1943**, *14*, 66–87. [CrossRef]
54. Cianfrocco, M.A.; Kassavetis, G.A.; Grob, P.; Fang, J.; Juven-Gershon, T.; Kadonaga, J.T.; Nogales, E. Human TFIID Binds to Core Promoter DNA in a Reorganized Structural State. *Cell* **2013**, *152*, 120–131. [CrossRef] [PubMed]
55. Kramm, K.; Schröder, T.; Gouge, J.; Vera, A.M.; Heiss, F.B.; Liedl, T.; Engel, C.; Vannini, A.; Tinnefeld, P.; Grohmann, D.; et al. DNA origami-based single-molecule force spectroscopy unravels the molecular basis of RNA Polymerase III pre-initiation complex stability. *bioRxiv* **2019**, 775528. [CrossRef]
56. Nelder, J.A.; Mead, R. A Simplex Method for Function Minimization. *Comput. J.* **1965**, *7*, 308–313. [CrossRef]
57. Arrhenius, S. Über die Dissociationswärme und den Einfluss der Temperatur auf den Dissociationsgrad der Elektrolyte. *Z. Für Phys. Chem.* **1889**, *4*, 96–116.
58. Arrhenius, S. Über die Reaktionsgeschwindigkeit bei der Inversion von Rohrzucker durch Säuren. *Z. Für Phys. Chem.* **1889**, *4*, 226–248.
59. Eyring, H. The Activated Complex in Chemical Reactions. *J. Chem. Phys.* **1935**, *3*, 107–115. [CrossRef]
60. Evans, M.G.; Polanyi, M. Some applications of the transition state method to the calculation of reaction velocities, especially in solution. *Trans. Faraday Soc.* **1935**, *31*, 875–894. [CrossRef]
61. Pihan, E.; Delgadillo, R.F.; Tonkin, M.L.; Pugnière, M.; Lebrun, M.; Boulanger, M.J.; Douguet, D. Computational and biophysical approaches to protein-protein interaction inhibition of Plasmodium falciparum AMA1/RON2 complex. *J. Comput Aided Mol. Des.* **2015**, *29*, 525–539. [CrossRef]
62. Delgadillo, R.F.; Parker, M.L.; Lebrun, M.; Boulanger, M.J.; Douguet, D. Stability of the Plasmodium falciparum AMA1-RON2 Complex Is Governed by the Domain II (DII) Loop. *PLoS ONE* **2016**, *11*, e0144764. [CrossRef]